Materials Today Catalysis 14 (2026) 100147

Contents lists available at ScienceDirect

Materials Today Catalysis

journal homepage: www.journals.elsevier.com/materials-today-catalysis

Effects of CuO-derived catalysts morphology on carbon dioxide electrochemical reduction in a flow cell

Falak Shafiq [a,1], Laura Vigni [b,2], Davide Melotto [a], Tatiana Rodríguez-Flores [a,3], Elizaveta Kozyr [c,4], Ivan Grigioni [b,5], Lorenzo Mino [c,6], Maria Vittoria Dozzi [b,7,*], Roberto Nisticò [a,8,*]

[a] Department of Materials Science, University of Milano-Bicocca, U5, INSTM, Via R. Cozzi 55, Milano 20125, Italy
[b] Dipartimento di Chimica, Università degli studi di Milano, Via C. Golgi 19, Milano 20133, Italy
[c] Department of Chemistry, INSTM and NIS Centre, University of Torino, via P. Giuria 7, Torino 10125, Italy

ARTICLE INFO

Keywords:
Carbon dioxide reduction reaction (CO_2RR)
Copper oxides
Electrocatalysis
Heterogeneous catalysis
Surface science

ABSTRACT

The electrochemical CO_2 reduction reaction (e-CO_2RR) represents a sustainable approach to convert CO_2 into valuable fuels and chemicals using renewable electricity to close the carbon loop and mitigate the climate change. In this scenario, oxide-derived Cu catalysts (*i.e.*, Cu oxides precursor modified by the application of a negative electrochemical bias to perform the CO_2 reduction) have emerged as promising materials for the e-CO_2RR, demonstrating an enhanced Faradaic Efficiency (FE) toward C_2 products, while significantly suppressing the CH_4 formation. In this work, CuO systems were synthesized using different soft-chemistry approaches (*i.e.*, precipitation vs. hydrothermal routes), and characterized through several advanced techniques such as TEM, SEM, XRD, BET analysis, Raman and FT-IR spectroscopies of adsorbed probe molecules. Catalytic performances were determined in terms of FE by monitoring the production of the main CO_2 reduction derivatives in a flow cell. By performing a systematic study, it was demonstrated that both starting CuO particles size and morphology represent critical factors determining the C−C coupling reaction, mandatory to obtain C_2 products. In particular, oxide-derived Cu catalysts presenting particles with sheet-like morphology showed superior selectivity for the CO_2 conversion into C_2 derivatives (*i.e.*, 50% at 200 mA cm^{-2}), with > 40% of C_2H_4 formation at high production rate (400 mA cm^{-2}). Interestingly, both CuO particles size increase and their morphological changes toward either tabular-prismatic or spheroidal shapes determine a substantial drop of the performances accompanied by a rise in the parasite hydrogen evolution reaction (HER).

1. Introduction

Nowadays, both the global environmental awareness [1,2] and the rapid depletion of the traditional fossil fuels [3,4] have moved the scientific community toward the search for novel, sustainable, and economically viable technologies able to exploit carbon sources alternative to petroleum for the production of chemicals/intermediates and/or fuels, destined for the industrial chemical synthesis and the energy sectors, respectively [5–9]. Among the available carbon sources, surely the main interesting and scientifically appealing one is carbon dioxide (CO_2) [10], which is the main relevant greenhouse gas having a key (detrimental) influence on the global climate change because of the

* Corresponding authors.
E-mail addresses: mariavittoria.dozzi@unimi.it (M.V. Dozzi), roberto.nistico@unimib.it (R. Nisticò).
[1] https://orcid.org/0009-0001-7347-3226
[2] https://orcid.org/0009-0005-9470-2066.
[3] https://orcid.org/0000-0003-2655-7715
[4] https://orcid.org/0000-0001-9308-5338
[5] https://orcid.org/0000-0002-9469-4570.
[6] https://orcid.org/0000-0002-9882-8361
[7] https://orcid.org/0000-0002-6390-9348.
[8] http://orcid.org/0000-0001-8986-5542

https://doi.org/10.1016/j.mtcata.2026.100147
Received 29 April 2026; Received in revised form 18 June 2026; Accepted 25 June 2026
Available online 28 June 2026

rapid increment of its release in the atmosphere at high concentrations, primarily due to the rapid industrialization progress [11–13].

Currently, the CO_2 molecule can be transformed into useful chemicals/fuels mainly through either catalytic [14] and photocatalytic [15] processes or biological microorganism-mediated routes [16]. Among these processes, the direct CO_2 reduction reaction through electrocatalysis (e-CO_2RR) has been extensively studied in recent years [17–20], mainly because of its high potential to transform CO_2 into many different value-added chemicals/intermediates/fuels by eventually utilizing electrons deriving from renewable energy resources (*e.g.*, integrating this technology with photovoltaics) [21,22].

At present, many metal and metal oxide electrocatalysts (ECs) have been employed (together with supporting materials) in the e-CO_2RR with good results. Promising ECs are metallic Fe [23], Co [24], Zn [25], Ni [26], and Cu [27], and oxides such as Cu/TiO_2 [28], FeO/CoO [29], ZnO [30], NiO [31], SnO_2 [32], as well as Cu oxides [33,34].

Since the key parameters driving the e-CO_2RR processes (namely, both the ECs' selectivity, expressed as Faradaic Efficiency, FE, and the thermodynamic potential) depend on the binding strength between the EC's metal site and the adsorbed species at the surface (*i.e.*, either CO_2 or intermediates/products), in the majority of the cases the design of the ECs is the process bottleneck. Among all the metal-based ECs, Cu is the only metal that has gained considerable attention in the field of electrocatalysis owing to its unique capacity of electrochemically reducing CO_2 into a number of oxygenates and hydrocarbon fuels, such as alcohols, aldehydes, and multi-carbon products [20,35]. In particular, Cu exhibits a proper CO adsorption capacity owing to its unique electronic structure able to promote the generation of both one-carbon (C_1) (*i.e.*, carbon monoxide (CO) [36], methane (CH_4) [37]) and multi-carbon (C_{2+}) products (*i.e.*, ethylene (C_2H_4), ethanol (C_2H_5OH) [38,39]), together with hydrogen (H_2; HER), which is the undesired e-CO_2RR parasite reaction [40]. Therefore, there is an intrinsic selectivity issue, making the catalytic process towards the synthesis of a specific double-carbon (C_2) compound difficult to be optimized. In fact, to reach this goal, the optimization of the ECs morphology and size, by altering surface characteristics [41,42] and exposing specific crystal facets, is found to be among the potential strategies available for the enhancement of C—C coupling and C_{2+} compound production [43]. In particular, C_{2+} products (*i.e.*, ethylene, ethanol, acetate, propanol, etc…) are very interesting chemical species from both the electrochemical and synthesis viewpoint, since they can store high-energy density and are important intermediates for a plethora of large-scale industrial processes (*e.g.*, light olefins are essential for the manufacturing of polymeric materials), respectively [44].

Generally, nanostructured ECs show considerable advantages over their bulk equivalents, including high surface-area, improved catalytic activity, and a high density of low coordination sites for efficient e-CO_2RR [45]. The general mechanism involved in the e-CO_2RR to produce C_{2+} products is a complex and multistep process involving many surface-bound species with different reactivity [20]. Even if the exact mechanism is still unclear and likely to vary along with a variety of reaction conditions, according to the literature there are four basic steps that should be considered when modeling such heterogeneous catalytic processes, namely:

1. The chemisorption of CO_2 molecules onto the ECs surface with formation of partially charged $*CO_2^{\delta-}$ species through interactions with surface metal atoms [46]. Physisorption of CO_2, a linear molecule, may occur simultaneously, which subsequently can be activated to a chemisorbed form via surface defects, alkali-metal promoted surfaces, or the electrons generated during the electrocatalysis [47,48].
2. The electron transfer and/or proton coupling processes, breaking the C—O bond, with the formation of additional reduced intermediates.
3. The formation of a C—C bond to produce a variety of C_{2+} compounds involving the production of hydrocarbons and oxygenated forms (*e.g.*, alcohols, aldehydes). This step is the most challenging one, as it requires a high coverage of C_1 intermediates generated during step 2.
4. The re-arrangement of the C-products followed by desorption from active sites and diffusion into the bulk electrolyte solution [49].

Operatively, in a typical electrolyzer, e-CO_2RR occurs at the cathode, while the oxygen evolution reaction (OER) takes place at the anode. The major cathodic reactions involved in the e-CO_2RR are summarized in Table 1 [20,50–53].

As previously introduced, Cu-based catalysts are very promising ECs since selective towards over a multitude of e-CO_2RR different products (namely, 16 reduction products, of which 12 being C_{2+}) [54]. Furthermore, the scientific literature pointed out that the presence of a certain oxidation state of Cu significantly improves the e-CO_2RR performance towards C_{2+} product conversion, evidencing how the co-presence of surface Cu(I) and O sites provides favorable binding sites capable of modulating the ECs' reactivity and selectivity [55]. In particular, it should be noted that in e-CO_2RR, Cu catalysts in oxidized form (*e.g.*, CuO) are "*in situ*" reduced by the application of the negative electrochemical bias into metallic Cu during the e-CO_2RR process, thus forming oxide-derived Cu catalysts (*i.e.*, OD-Cu; Cu oxide precursors modified during the e-CO_2RR) [55,56].

Over the years, several studies have been carried out to verify the intrinsic relationship between the structure of the ECs and their catalytic properties, considering various structural features, including the EC's morphology. For instance, Ren *et al.* [57] highlighted how the presence of Cu(I) ions on the surface of the EC allows an improved selective toward the formation of C_{2+} products compared to HER, with a FE of 34.3% for C_2H_4 and 16.4% for C_2H_5OH. Theoretical calculations have also shown that, when both Cu(0) and Cu(I) sites are present on the EC's surface, the synergistic effect between these two species facilitates the CO_2 activation process and the CO dimerization, thus enhancing the process selectivity toward C_2 products [58,59]. Moreover, even the O-atoms defectivity on the surface of the ECs is a very important aspect that should be considered. In this regard, Mistry *et al.* [58] demonstrated how CuO particles treated with plasma and characterized by O-atoms defects on the surface showed improved selectivity for the CO_2-to-C_2H_4 reduction (> 60% FE).

Regarding the role played by structural and/or surface properties, ECs with different morphologies exhibit different crystal planes, which can generate a different pH near the electrode, thus consequently

Table 1
Major eCO_2RR, and relative thermodynamic equilibrium potentials with respect to the Reversible Hydrogen Electrode (RHE) in aqueous electrolyte at pH 0, 1 atmospheric pressure, and 25 °C.

Reduction products	Electrochemical reactions	Reduction potential E^0 (V) *vs.* RHE
Carbon monoxide, CO	$CO_{2(g)} + 2H^+ + 2e^- \rightarrow CO_{(g)} + H_2O_{(l)}$	−0.11
Formic acid, HCOOH	$CO_{2(g)} + 2H^+ + 2e^- \rightarrow HCOOH_{(aq)}$	−0.12
Methanol, CH_3OH	$CO_{2(g)} + 6H^+ + 6e^- \rightarrow CH_3OH_{(aq)} + H_2O_{(l)}$	+0.03
Methane, CH_4	$CO_{2(g)} + 8H^+ + 8e^- \rightarrow CH_{4(g)} + 2H_2O_{(l)}$	+0.17
Acetic acid, CH_3COOH	$2CO_{2(g)} + 8H^+ + 8e^- \rightarrow CH_3COOH_{(aq)} + 2H_2O_{(l)}$	+0.11
Acetaldehyde, CH_3CHO	$2CO_{2(g)} + 10H^+ + 10e^- \rightarrow CH_3CHO_{(aq)} + 3H_2O_{(l)}$	+0.06
Ethylene, C_2H_4	$2CO_{2(g)} + 12H^+ + 12e^- \rightarrow C_2H_{4(g)} + 4H_2O_{(l)}$	+0.08
Ethanol, C_2H_5OH	$2CO_{2(g)} + 12H^+ + 12e^- \rightarrow C_2H_5OH_{(aq)} + 3H_2O_{(l)}$	+0.09
Ethane, C_2H_6	$2CO_{2(g)} + 14H^+ + 14e^- \rightarrow C_2H_{6(g)} + 4H_2O_{(l)}$	+0.14
Hydrogen (HER), H_2	$2H^+ + 2e^- \rightarrow H_2$	0.00

varying both nature and concentration of reaction intermediates/products [60]. In this regard, various theoretical studies have shown that the presence of {100} crystal planes of metallic Cu is advantageous for the e-CO_2RR as favors the C—C coupling reaction leading to C_{2+} products [61]. Recently, Wu *et al.* [62] synthesized metallic Cu nanoparticles containing both Cu{100} and Cu{111} crystal planes. Electrochemical tests demonstrated an increased selectivity toward C_{2+} products (*ca.* 75% FE at 300 mA cm^{-2} current density), compared to analogous systems containing isolated Cu{100} and Cu{111} crystal planes. Such behavior seems due to the presence of Cu{100}/Cu{111} interface, characterized by an electronic structure capable of promoting greater CO intermediate adsorption, and lowering the dimerization and C—C coupling energy. Additionally, high Miller index morphologies (*e.g.*, ECs presenting Cu{511}, Cu{711}, and/or Cu{911} crystal planes) are characterized by a high number of under-coordinated Cu atoms, and results being more selective for C_{2+} products compared to their analogous low Miller index counterparts (*e.g.*, Cu systems presenting only {100} crystal planes) [63,64]. Ma *et al.* [65] prepared CuO-based nanowires produced by calcining $Cu(OH)_2$ nanowires at 150 °C, and tested them as ECs for the e-CO_2RR, observing an increment of the selectivity toward C_2 products with the nanowire size. In general, the longer the average length of the nanowires, the lower the bicarbonate ions' diffusion in solution, and consequently the higher the selectivity toward high C-containing products. Loiudice *et al.* [66], instead, evaluated the effect of both morphology and size by comparing the electrochemical performances of metallic Cu nanospheres and nanocubes at different size, observing for both morphologies an increase in selectivity towards C_2H_4 when reducing the average particle size, with an improved selectivity toward C_2 products when employing nanocubes. Authors attributed this specific trend to the higher number of low-coordination sites available when reducing the nanocubes size. Finally, the presence of porosity and three-dimensionality are also important parameters influencing the selectivity towards C_{2+} products, as both influence the local pH, the residence time of the intermediate, the gas permeability, and the liquid diffusion rate [67].

Despite the extensive literature demonstrating the main role of Cu-based nanostructures for enhancing the e-CO_2RR, the relative contribution due to the EC's morphology, surface active sites, and gas diffusion layer organization remains poorly understood. In this regard, a plethora of scientific studies have focused on EC architectures as key descriptors governing the e-CO_2RR selectivity [17,18,20], whereas fewer studies investigated the influence of operating conditions [21,22], or structural organization, coverage uniformity, and transport properties of the EC layer on the gas diffusion electrode [28]. In this study, the present authors address this gap through a systematic investigation employing different oxide-derived Cu catalysts (*i.e.*, CuO ECs before the application of the negative electrochemical bias) prepared via scalable soft-chemistry methods, namely precipitation and hydrothermal route, with distinct morphologies, namely sheet-like, spheroidal, and tabular-prismatic structures. By combining several advanced techniques such as TEM, SEM, XRD, BET analysis, Raman spectroscopy, FT-IR spectroscopy of adsorbed CO to investigate the surface Cu active sites, and electrochemical analyses, it was evidenced the direct correlations between the initial EC morphology, exposed Cu surface sites, EC layer organization on gas diffusion electrodes, and the attained e-CO_2RR performance. Results demonstrate that the superior selectivity (quantified as FE) toward the C−C coupling reaction, mandatory to obtain C_2 products is primarily due to the 2D sheet-like morphology, whereas tabular-prismatic and/or spheroidal shapes determine a substantial drop of the performances accompanied by a rise of the undesired HER. However, such superior selectivity results from the combination of several factors, such as the surface accessibility, Cu surface environments, and the formation of a homogeneous EC network promoting C–C coupling reactions. These findings provide additional insight into the design principles governing oxide-derived Cu catalysts for selective e-CO_2RR.

2. Material and methods

2.1. Chemicals

Reactants: Copper(II) nitrate trihydrate ($Cu(NO_3)_2{\cdot}3H_2O$, puriss. p.a., 99% purity, CAS 10031–43−3, Thermo Scientific). Solutions and solvents: different NaOH solutions were prepared by dissolving sodium hydroxide pellets (NaOH, puriss., p.a., ACS reagent, ≥ 98%, CAS 1310–73−2, Aldrich) in deionized water, whereas acetone (CAS 67–64−1, Sigma-Aldrich) was used as it is. Deionized water was used during washing procedures. Milli-Q water with a resistivity of 18.2 MΩ cm was used. All chemicals were used without further purification. Ink preparation: 2-propanol (anhydrous, 100%, CAS 67–63−0, VWR Chemicals Avantor), Nafion™ solution (PFSA 5 wt%, CAS 31175–20−9, Qintech), PET-reinforced anion exchange membrane (thickness: 130 μm, Qintech), Freudenberg H23 gas diffusion layers (Qintech). Electrochemical tests: CO_2 cylinder (5 L, 99.995%, Sapio), potassium hydroxide (KOH, 90%, CAS 1310–58−3, Sigma-Aldrich). Preparation of ^{1}H NMR samples for liquid products analysis: deuterium oxide (D_2O, 99.9%, CAS 7789–20−0, Sigma-Aldrich), dimethyl sulfoxide (99.9%, CAS 67–68−5, Sigma-Aldrich).

2.2. Synthesis of CuO via hydrothermal route: tabular-prismatic particles

CuO material with prismatic tabular morphology is obtained through hydrothermal route following a modified procedure from the literature [68]. In particular, a copper(II) nitrate solution (2.7 g in 37.5 mL of deionized water) was stirred for 30 min at a temperature of 40 °C. Subsequently, while maintaining the solution in constant agitation, a 6 M NaOH solution is added dropwise to the prepared solution until a pH of around 12 is reached (Vol. approx. 37.5 mL). This way, a black precipitate of CuO is formed at the bottom of the reaction vessel.

The obtained solution (Total Vol. approx. 75 mL) is transferred into a 125-mL sealed Teflon-lined autoclave Model 4748 (*Parr Instrument Company, Illinois, USA*). The autoclave is hermetically sealed in order to prevent liquid spillage, and thermally treated in a Carbolite CWF1200 muffle furnace (*Carbolite, Hope, UK*) with the following thermal program: (i) heating ramp from RT to 200 °C (heating rate: 10 °C min^{-1}), (ii) isothermal step at 200 °C for 10 h, and (iii) cooling step from 200 °C to 50 °C (cooling rate: 5 °C min^{-1}).

Once the reaction is completed, the autoclave is removed from the furnace and naturally cooled to RT. The solution is then transferred into a Falcon tube for centrifugation (6000 rpm, 10 min), and washed 3 times with deionized water and once with acetone.

The final precipitate is oven dried under air atmosphere at 80 °C overnight. Lastly, the dried solid is gently crumbled inside an agate mortar, and sample storage inside a closed glass vial.

The obtained sample is defined as H-TP (CuO sample from 6 M NaOH solution, after hydrothermal route), where "H" indicates the hydrothermal route and "TP" refers to the tabular-prismatic shape of the particles.

2.3. Synthesis of CuO via precipitation route: spheroidal particles

CuO material with spheroidal morphology is obtained through precipitation route following a modified procedure from the literature [69]. In particular, a copper(II) nitrate solution (2.4 g in 50 mL of deionized water) was prepared in a reaction flask under constant agitation for about 2 min at RT. Subsequently, a 0.25 M NaOH solution is added dropwise (rate 5 mL min^{-1}) to the prepared solution (vol. 50 mL). The solution is heated to 80 °C and maintained under constant stirring for 0.5 h. Once the reaction is completed, the solution is allowed to naturally cool down to RT. The solution is then transferred into a Falcon tube for centrifugation (6000 rpm, 10 min), and washed 3 times with deionized water and once with acetone.

The final precipitate is oven dried under air atmosphere at 80 °C

overnight. Since in this case it is registered the formation of a bluish-white precipitate, indicating the formation of copper(II) hydroxide-nitrate ($Cu_2(OH)_3NO_3$), the solid is transferred into an alumina crucible and thermally treated in a Carbolite CWF1200 muffle furnace (*Carbolite, Hope, UK*) with the following thermal program: (i) heating ramp from RT to 700 °C (heating rate: 10 °C min^{-1}), (ii) isothermal step at 700 °C for 5 h, and (iii) cooling step from 700 °C to 50 °C (cooling rate: 5 °C min^{-1}). Lastly, the dried solid is gently crumbled inside an agate mortar, and sample storage inside a closed glass vial.

The obtained sample is defined as PT-Sp (CuO sample from precipitation route employing a 0.25 M NaOH solution, after thermal treatment), where "P" indicates the precipitation route, "T" indicates that the sample is thermally treated, and "Sp" refers to the shape of the particles, namely spheroidal.

2.4. Synthesis of CuO via precipitation route: large sheet-like particles

CuO material with sheet-like morphology is obtained through a precipitation route following a modified procedure from the literature [69]. In particular, a copper(II) nitrate solution (2.4 g in 50 mL of deionized water) was prepared in a reaction flask under constant agitation for about 2 min at RT. Subsequently, a 1 M NaOH solution is added dropwise (rate 5 mL min^{-1}) to the prepared solution (vol. 50 mL). The solution is then heated to 80 °C and maintained under constant stirring for 0.5 h. Once the reaction is completed, the solution is allowed to naturally cool down to RT.

The sample obtained employing such NaOH concentration shows the formation of black precipitates indicating the direct formation of CuO. The solution is then transferred into a Falcon tube for centrifugation (6000 rpm, 10 min), and washed 3 times with deionized water and once with acetone.

The final precipitate is oven dried under air atmosphere at 80 °C overnight. Lastly, the dried solid is gently crumbled inside an agate mortar, and sample storage inside a closed glass vial.

The obtained sample is defined as P-Sh (CuO sample from precipitation route employing a 1 M NaOH solution), where "P" indicates the precipitation route, and "Sh" refers to the shape of the particles, namely sheet-like.

2.5. Characterizations

X-ray powder diffraction (XRD) patterns were recorded by means of a Rigaku Miniflex 600 at the University of Milano-Bicocca. The acquisition was performed using a Cu source (40 kV, 15 mA), scanning in the 10–80° 2θ range, with a step size of 0.02°, angular velocity 5.0° per minute. Instrumental PDXL−2 software was used for the sake of comparison with reference diffraction patterns from the ICDD database. The crystallite average size was estimated by means of the Debye-Scherrer equation (Equation (1)):

$$d = \frac{k\lambda}{\beta \cos\theta} \quad (1)$$

where d is the average size of the crystalline domains (expressed in nm), K is the shape factor (typically 0.9), λ is the X-ray wavelength (0.154 nm for a Cu source), β is the line broadening at half the maximum intensity (FWHM) of the selected Bragg angle after subtracting the instrumental line broadening (expressed in radians), and θ is the Bragg angle (expressed in radians). Regarding the CuO systems, the Bragg angle selected was the crystal reflection at *ca.* $2\theta = 35.6°$ corresponding to the Miller index (−111).

Scanning electron microscopy (SEM) micrographs of powder ECs were collected by means of a Zeiss Gemini 500 microscope at the University of Milano-Bicocca equipped with a traditional secondary electrons' detector. Samples were deposited onto SEM stubs using a double-adhesive carbon tape for SEM analysis. Stabs were covered with a gold coating to prevent any charging effect by means of a VPI SD–900 C sputter coater. Particle size distribution was performed by using ImageJ software, analyzing more than 50 particles per micrograph. SEM images of GDEs have been acquired at the University of Milan by using a FE-SEM Sigma (Zeiss, Germany) operating at 5 kV with a working distance of 5 mm and an Inlens detector. The electrodes were platinum coated by an EM ACE 600 (Leica Microsystem, Germany).

Transmission electron microscopy (TEM) analysis was carried out by means of a FEI TECNAI G2 F20 electron microscope of the Unitech COSPECT at the University of Milan, operating at an accelerating voltage of 200 kV, with a Gatan CCD camera allowing high-resolution imaging. Few mg of the specimens were sonicated in 2-propanol and then transferred as a suspension on a copper grid covered with a holey carbon film. Micrographs were taken after solvent evaporation, spanning over the whole region of the sample, to achieve a truly representative statistical mapping of the investigated materials.

N_2 adsorption-desorption isotherms were recorded at 77 K using a Micromeritics ASAP analyzer. Prior to analysis, the samples were degassed under vacuum at 120 °C. The specific surface area (SSA) was determined applying the Brunauer–Emmett–Teller (BET) model.

Fourier Transform infrared (FT-IR) spectroscopic measurements were performed in transmission mode with a resolution of 2 cm^{-1} on a Bruker INVENIO FTIR spectrometer equipped with a MCT detector. Samples were prepared as self-supporting pellets with an optical density of *ca.* 13 mg·cm^{-2} and placed in a custom-made quartz IR cell with KBr windows. Prior to measurements, each sample was outgassed at 200 °C for 1 h, reaching a residual pressure of *ca.* $5 \cdot 10^{-4}$ mbar. IR spectra of adsorbed CO were then recorded at liquid nitrogen temperature. The spectra were normalized to the optical density of the pellet.

Raman spectra were acquired using a Renishaw inVia Raman Microscope spectrometer, equipped with a 1800 lines mm^{-1} grating and CCD detector. The excitation source was an Ar^+ laser emitting at 514 nm. The excitation beam was focused on the sample through a 50 × objective lens. All the spectra were acquired using 10% of laser power (corresponding to 0.5 mW), accumulating 20 spectra of 30 s each.

2.6. Gas diffusion electrode (GDE) preparation

Gas diffusion electrodes (GDE) were prepared by spray coating catalyst ink onto hydrophobic carbon paper (C paper, Freudenberg H23C8). The ink was prepared by suspending 10 mg of ECs powder in 10 mL of isopropanol for 20 min of sonication. Then, a known amount (50 μL) of Nafion™ solution was added, followed by sonication for 10 min at RT. The as-prepared ink was sprayed on a 3 × 3 cm^2 GDL employing an airbrush gun (Paasche H3AS) with a 0.635 mm nozzle. To guarantee the uniformity and reproducibility of the catalyst layer the GDL was positioned vertically at *ca.* 3 cm from the nozzle, and the spraying direction was changed frequently, back and forth. To study the effect of the ECs loading on the final performance in CO_2RR, electrodes were prepared for each sample with three different amounts of EC powder: low (1–2 mg), medium (3–4 mg), and high loading (5–6 mg). The exact amount of EC deposited was determined by accurate weighing. Each electrode was thus labelled as X_Y, where: "X" refers to the sample code of the investigated material, whereas "Y" indicates the low (l), medium (m), or high (h) catalyst amount.

2.7. Electrocatalytic measurements

The measurements have been carried out using an electrochemical station (Metrohm Autolab PGSTAT204) connected with a flow cell system. The EC material assembled in a GDE (a described in Section 2.6) was used as the cathode, while an Ag/AgCl electrode (CH Instruments) and Ni foam were employed as reference and counter anode electrode, respectively. In this electrochemical configuration, the parallel disposition of the working and the counter electrode ensures a uniform potential distribution across the cell. The anode and cathode electrodes are

2 cm apart, resulting in a high ohmic resistance that prevents meaningful measurement of the full-cell potential in this configuration. The catholyte and anolyte compartments were filled with a 1 M KOH solution, which was recirculated continuously by a peristaltic pump. CO_2 gas was fed from the backside (the side without the catalytic material) of the gas-diffusion electrode at a flow rate of 50 sccm. An anion-exchange membrane, PET-reinforced (Quintech), was used to separate the anodic and cathodic compartments to avoid oxidation of CO_2RR products at the anode.

Gaseous products were sampled with a gastight syringe and analyzed with an Agilent 8860 gas chromatograph equipped with a thermal conductivity detector (TCD), a flame ionization detector (FID), and two columns, one Coarboxen (to separate permanent gases) and a molecular sieve (MS, to separate C_1-C_4 products) columns. The GC was calibrated for H_2, CO, CH_4, and C_2H_4. Two standard gas mixtures (Sapio) were used for calibration. Ultra-pure Ar (grade 5) was employed as carrier gas. The TCD was used to detect hydrogen (H_2), oxygen (O_2), nitrogen (N_2), and carbon monoxide (CO), while the FID detector was employed to determine methane (CH_4), ethylene (C_2H_4), and, eventually, carbon dioxide (CO_2) through a methanizer.

The Faradaic Efficiency (FE) for the gaseous product is calculated with the following equation (Equation (2)):

$$FE = \frac{n_e \times F \times C \times f}{V_M \times I} \quad (2)$$

where n_e is the number of electrons required to reduce CO_2 to each product, F is the Faraday constant, C is the product concentration in the gas stream obtained from GC analysis (in ppm), f is the flow rate (sccm), V_M is the normal molar volume (24.1 L/mol) and I is the absolute value of the imposed current densities (mA cm^{-2}), ranging from 50 up to 400 mA cm^{-2} and representing the reaction rate in the electrocatalytic systems. In particular, the system has been kept at each chosen current density for at least 5 min, allowing the obtainment of an almost constant working electrode potential, which has been continuously monitored, up to a total measurement time of *ca.* 25 min, as represented in Figure S1. The potential vs. Ag/AgCl values were converted into the RHE scale using the following equation: $E_{RHE} = E_{AgCl} + 0.059\ pH + E_{AgCl}^{\circ}$, with E_{AgCl}° (3 M KCl) = 0.210 V at 25 °C.

Each FE value has been determined by averaging the results obtained by performing two consecutive GC analysis at each fixed applied current density.

Stability properties of selected GDE electrodes have been preliminary checked by monitoring the e-CO_2RR at the highest reaction rate (400 mA cm^{-2}) up to a maximum time of 3 h.

The FE for liquid products has been determined for selected samples by quantitative ^{1}H NMR analysis. In particular, a volume of 0.2 mL of catholyte, anolyte and cold aqueous trap (collecting species possibly stripped by the CO_2 flow) was sampled after a specific reaction time and mixed with 0.1 mL of a 500 ppm DMSO solution (as the internal standard) and 0.4 mL of D_2O. The mixture was analyzed with ^{1}H NMR. The equation used for the calculation of the liquid products FE is (Equation (3)):

$$FE = \frac{n_e \times F \times C}{V \times I \times t} \quad (3)$$

where n_e is the number of electrons required to reduce CO_2 to each product, F is the Faraday constant, C is the product concentration obtained from ^{1}H NMR (in ppm), V is the total volume of the electrolyte, I is the current (mA) and t is the duration of electrolysis (usually 2000 s at 200 mA cm^{-2}). The liquid products evaluation has been performed twice and averaged. The uncertainty associated to the calculated mean FE values resulted to be lower than 5%.

3. Results and discussion

3.1. Structural, morphological and physicochemical characterization of the CuO ECs

Fig. 1 reports the XRD performed on the investigated materials. In general, in all cases (*i.e.*, H-PT, PT-Sp, and P-Sh) the presence of diffraction peaks at *ca.* 2θ = 32.5° (110), 35.6° (−111), 38.8° (111), 46.3° (−112), 48.7° (−202), 51.4° (112), 53.5° (020), 58.4° (202), 61.6° (−113), 65.9° (022), 66.3° (−311), 68.2° (220), 72.5° (311), and 75.3° (−222) confirms the presence of the monoclinic crystal phase of CuO (ICDD 01–080−1268), in agreement with the literature (Fig. 1) [70]. Interestingly, as reported in Sections 2.2, 2.3, and 2.4, both H-PT and P-Sh samples are directly synthesized in their CuO crystal form, whereas PT-Sp sample, instead, initially precipitates as $Cu_2(OH)_3NO_3$. The XRD analysis registered for this intermediate form reveals the presence of diffraction peaks at *ca.* 2θ = 12.8° (001), 21.6° (110), 25.8° (002), 32.0° (200), 33.6° (−201), 36.5° (121), 39.8° (−202), 41.9° (013), 43.5° (122), 49.2° (−131), 51.4° (−123), 53.4° (123), 58.7° (−321), 60.8° (033), and 62.4° (041) attributable to the presence of the crystal phase of $Cu_2(OH)_3NO_3$ (ICDD 01–075−1779), and in agreement with literature (Figure S2b, *SI*) [71]. After performing the thermal treatment under air atmosphere, this intermediate form evolves toward the formation of the CuO crystal form, as demonstrated by the XRD analysis (Fig. 1).

The analysis of the cell parameters (*a, b, c*), and the average crystallite size (*d*) calculated by employing the Debye-Scherrer equation for all CuO samples is summarized in Table 2.

In general, similar values of cell parameters are registered for all the three samples. Conversely, the calculated average crystallite size varies significantly with the sample preparation. In fact, regarding the precipitation route, the average crystallite size of PT-Sp sample (obtained employing 0.25 M NaOH, but after performing a thermal treatment at high temperature) is remarkably higher compared to the value calculated for P-Sh sample (obtained employing 1 M NaOH, but without performing a thermal treatment at high temperature), showing *ca.* 50 nm, and *ca.* 23 nm size, respectively. This phenomenon might be attributable to the effect played by the higher annealing temperature, favoring the grain growth of the final material [72].

Lastly, H-TP sample (obtained by means of hydrothermal route at 200 °C employing 6 M NaOH) shows the highest average crystal size of *ca.* 70 nm. Since hydrothermal routes are based on crystallization reactions happening into sealed autoclaves at temperatures in the

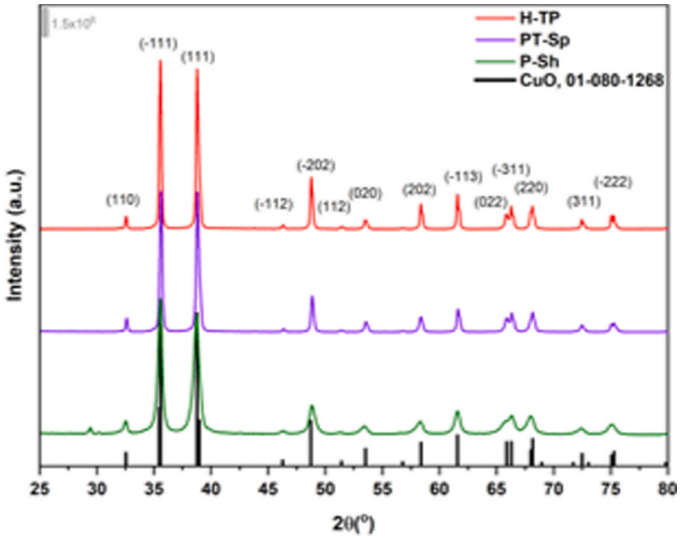

Fig. 1. XRD patterns of the investigated ECs, namely: H-TP sample (red, top), PT-Sp sample (violet, middle), and P-Sh sample (green, bottom). XRD reference pattern: tenorite (CuO, 01−080−1268, black).

Table 2
Average crystallite size and lattice parameters determined by XRD analysis, and calculated BET SSA values for the three CuO ECs.

Samples	*d* (nm)	a (Å)	b (Å)	c (Å)	BET SSA ($m^2 g^{-1}$)
H-TP	70	4.68	3.42	5.13	< 1
PT-Sp	50	4.68	3.42	5.12	< 1
P-Sh	23	4.69	3.43	5.14	15

150–300 °C range and relatively high pressure, it is expected a crystallinity increase of the resultant material, in accordance with the literature [73].

Fig. 2 reports SEM and TEM morphological characterizations of the three CuO investigated materials, whereas particle size distribution (calculated by analyzing the SEM micrographs) is reported in Figure S2. As shown in Figs. 2**a** and 2**b**, H-TP sample is composed by crystal aggregates with a tabular-prismatic shape and length in the 0.5–1.5 μm range according to both TEM and SEM analysis (Figure S3, *SI*). Differently, the PT-Sp sample precursor was characterized by the formation of irregularly shaped particle aggregates with mean size in the 60–250 nm range (Figure S2a, *SI*) Interestingly, upon the application of the reported thermal treatment, PT-Sp sample resulted to be composed by irregular spheroidal particles, with dimensions dispersed in the relatively wide 0.2–1.0 μm range (Figs. 2**c**, and 2**d**) according to both TEM and SEM analysis (Figure S3, *SI*). Lastly, in the case of P-Sh samples, SEM analysis clearly reveals the formation of two-dimensional particle aggregates, exhibiting a peculiar sheet-like morphology, with an average thickness of *ca.* 40 nm and a mean 0.8–1.5 μm length size (Figs. 2**e**, and 2**f**) according to both TEM and SEM analysis (Figure S3, *SI*).

In agreement with the microscopy data and with the average crystallite sizes obtained from XRD analysis, P-Sh sample exhibits a reasonably high BET specific surface area, whereas it is much more limited for PT-Sp and H-TP samples (Table 2). Therefore, the morphological characterization evidenced that the three selected samples are characterized by the same CuO bulk crystal structure, sub-micrometric particle size (following the order P-Sh > H-TP > PT-Sp, with P-Sh having a nanometric thickness), but significantly different particle aggregates morphology, passing from irregularly spheroidal toward tabular-prismatic or two-dimensional sheet-like shapes for the PT-Sp, H-TP and P-Sh samples, respectively.

3.2. *Electrocatalytic CO_2RR testing*

Electrochemical results obtained with the investigated GDEs containing variable EC loadings (either low, medium or high) are reported in Fig. 3 in terms of Faradaic Efficiencies (FEs) toward gaseous CO_2

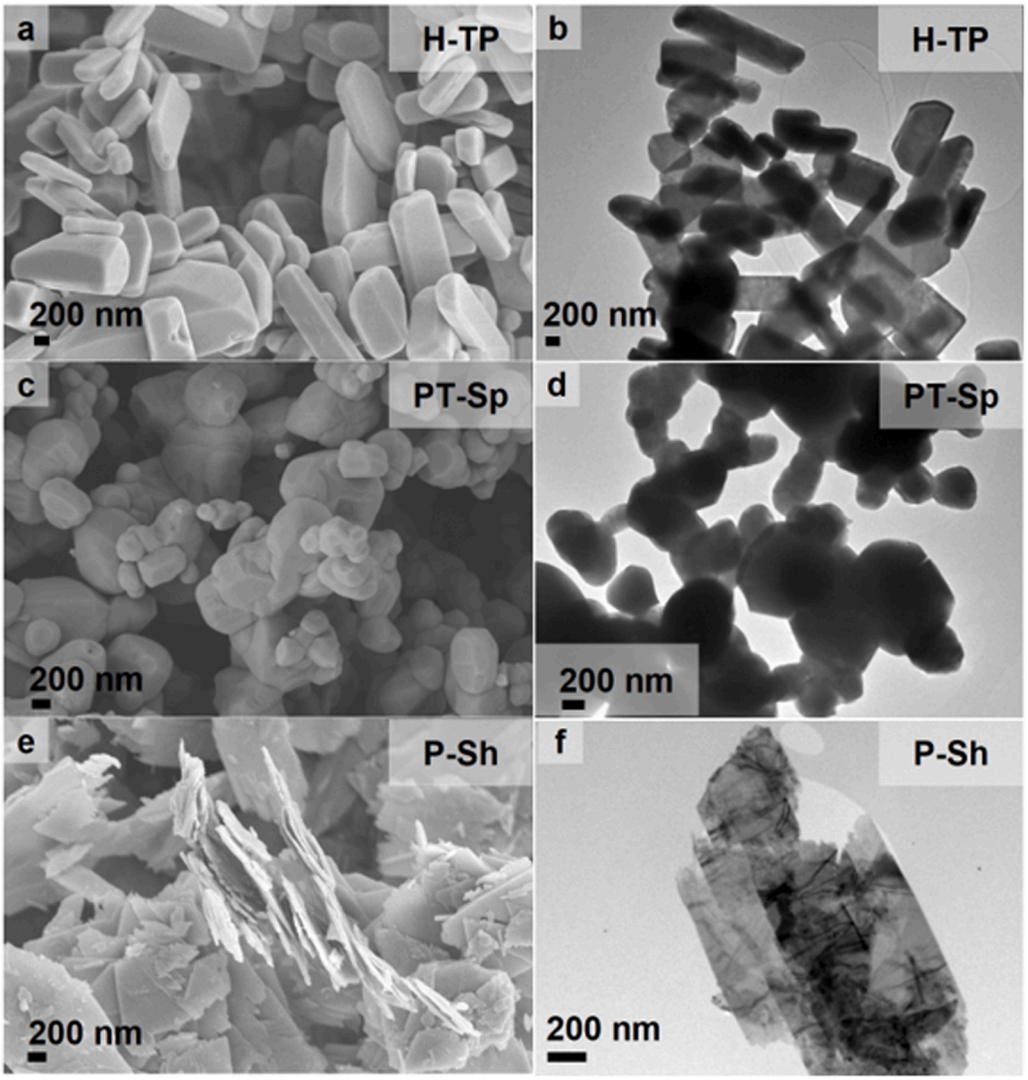

Fig. 2. SEM (left) and TEM (right) micrographs of the investigated ECs, namely: Panels (a, b) H-TP sample (hydrothermal route; top), (c, d) PT-Sp sample (precipitation route with 0.25 M NaOH and thermal treatment; middle), and (e, f) P-Sh sample (precipitation route with 1 M NaOH; bottom).

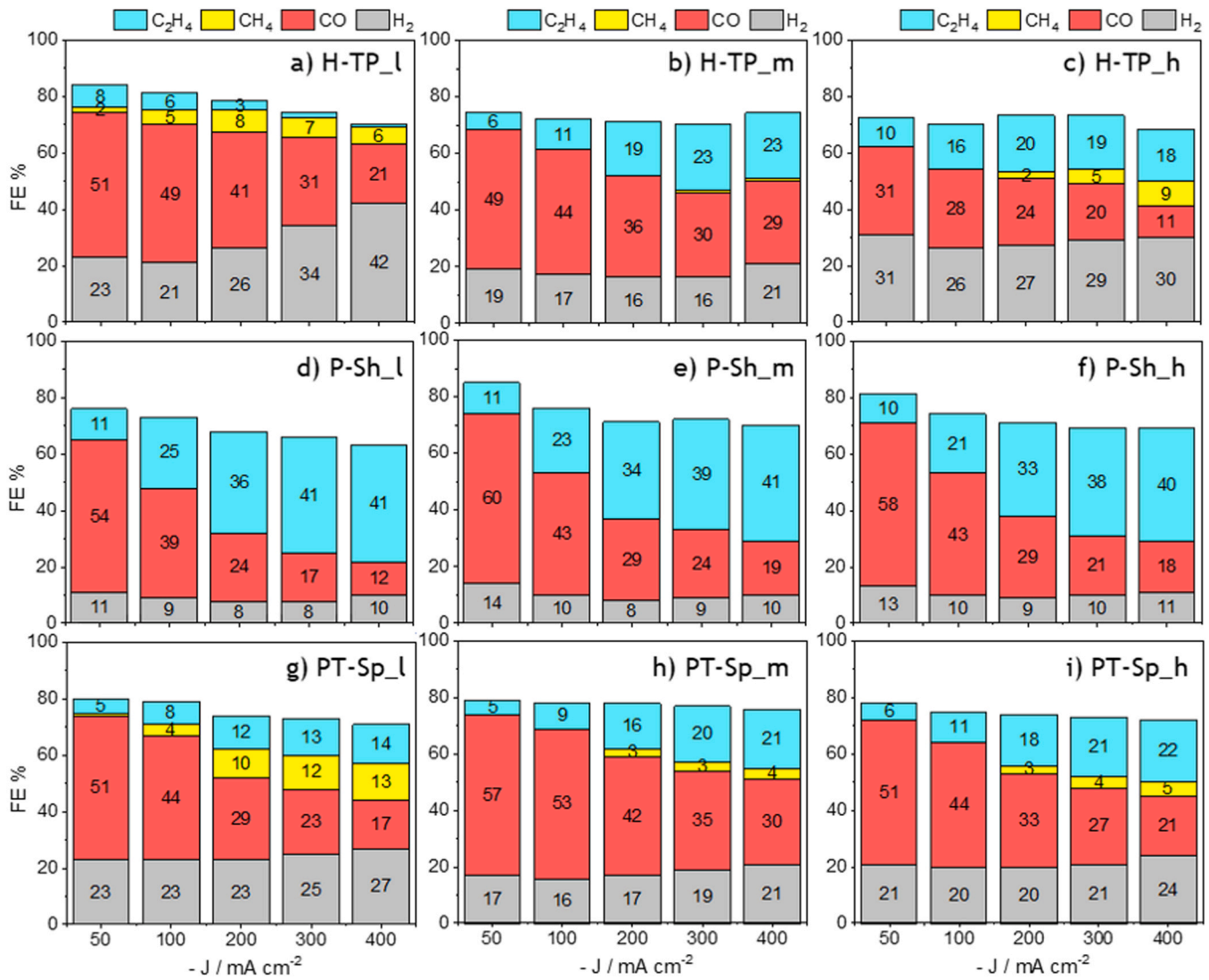

Fig. 3. Faradaic Efficiencies (FE) toward gas products (ethylene, carbon monoxide, methane, and hydrogen) during the electrocatalytic CO_2 reduction at different current densities (100, 200, 300, and 400 mA cm^{-2}) obtained with (a-c) H-TP, (d-f) P-Sh and (g-i) PT-Sp samples at low (left data column), medium (middle data column) and high (right data column) loading.

reduction products.

The FEs obtained with H-TP sample, synthesized via the hydrothermal method, confirm the good efficiency of CuO NPs in catalyzing the electrochemical CO_2RR, manly toward CO production, in line with what already established in the literature [74–76], though the undesired H_2 production resulted to be quite significant, especially at relatively low catalyst loading (1–2 mg), where the FE toward H_2 reaches values of *ca.* 30%, probably due to a low catalyst surface exposure of active sites available for promoting the CO_2RR. At the same time, the progressive increase of ECs loading significantly promotes the ethylene formation (almost independently on the applied current density), although the total FE for CO_2 reduction tends to diminish, probably due to a relatively higher electrical and CO_2 diffusion resistance attained with the thicker catalyst layer (CL). In fact, both SEM and TEM images evidenced that H-TP sample is characterized by large and densely packed particles. It is well known that both geometry and morphological features of the CL can affect CO_2 transport properties within the GDE and, thus, the overall performance in terms of FEs for CO_2RR [77,78].

Optimal results have been attained with the GDE prepared by employing a medium (3–4 mg) catalyst loading (Fig. 3**b**), possibly allowing the obtainment of a proper metal oxide layer thickness guaranteeing an optimized electrical transfer and CO_2 diffusion.

Interestingly, the P-Sh sample, characterized by a sheet-like morphology, exhibits completely different catalytic properties, with an extremely relevant ethylene production (FE of 35–40%) on the whole investigated catalyst loading range and almost independently on the applied 200–400 mA cm^{-2} current density range. In particular, the almost exclusive CO production (FE of 60–70%) at low current densities tends to decrease in favor of ethylene production by increasing the applied current density, as expected for the C–C coupling pathway, *i.e.* CO being considered as the major intermediate for the formation of C_{2+} hydrocarbons via CO_2RR. In fact, according to both experimental research and density functional theory (DFT) calculations, *CO–*CO coupling is the most kinetically favorable pathway for C–C coupling leading to C_{2+} reduction products on Cu-based catalysts [79]. For this reason, the accumulation of a high local concentration of CO species on the catalyst surface is necessary to enable the coupling and, consequently, the production of ethylene. This condition is achieved particularly efficiently at high current densities, when the CO_2RR proceeds more rapidly, thus resulting in a higher local production of activated intermediates.

P-Sh sample ensures a total conversion towards gaseous products above 70% with a very high selectivity corresponding to the quite exclusive production of ethylene, with a FE above 40% at 400 mA cm^{-2}

in 1 M KOH electrolyte. Importantly, the beneficial effect intrinsically played by the CuO sheet-like morphology in favoring ethylene production, also allowing stable catalytic activity, is demonstrated by the fact that P-Sh sample guarantees similar and satisfying performances across all the three investigated catalyst loadings (1–5 mg).

Differently, thermally treated PT-Sp sample shows an intermediate catalytic activity between those shown by H-TP and P-Sh samples. In particular, the total conversion towards gaseous species remains consistently stable at *ca.* 80%, with CO being the predominant product. As in the previous cases, ethylene production increases with increasing the applied current density; however, the highest attained FE for C_2H_4 corresponds to *ca.* 20% and is almost half of that exhibited by the sheet-like P-Sh sample under similar experimental conditions (*i.e.*, by applying 400 mA cm^{-2} current density with a medium or high catalyst loading). The undesired and competitive hydrogen production results instead to be favored and almost double compared to that attained with the best performing P-Sh catalyst (see Fig. 3**h** vs. Fig. 3**e**).

Therefore, PT-Sp sample shows broader products distribution and lower ability toward CO_2 (instead of water) electroreduction on the whole investigated catalyst loading range. This finding may be related to the CuO particles morphological changes from sheet-like structures to irregular spherical shapes observed upon the applied heating procedure.

In this scenario, De Gregorio *et al.* [80] found a crucial role played by Cu nanoparticles shape among spherical, octahedral, and cubic morphology in affecting the overall CO_2RR activity. In particular, 44 nm-length Cu cubes achieved the highest selectivity toward CO_2RR, with a total FE of 80% and selectivity for ethylene of *ca.* 41% in a flow-cell electrolyzer and the authors suggested the optimal ratio between edge and (100) plane sites (of *ca.* 0.25), attained with such material, as a crucial structural parameter for controlling the CO_2RR product selectivity [80].

Interestingly, in our investigation only PT-Sp sample exhibits a detectable production of methane, with a maximum of FE of *ca.* 13% at 400 mA cm^{-2} with a low catalyst loading (Fig. 3**g**). This observation suggests a possible effect induced by the electrode polarization. It has been reported that at high overpotentials (more negative than −0.8 V vs. RHE), both ethylene (C_2H_4) and methane (CH_4) can form simultaneously from the common COH intermediate on Cu (100) and Cu (111) facets [63,81], though this behavior has not been generally observed in alkaline media [81–83]. We thus hypothesize that the relatively more negative potential required to achieve the target current density at low (1–2 mg) catalyst loading, where the exposed catalyst surface is limited, may favor methane over ethylene formation. This change of selectivity may be attributed to modifications in the local reaction environment under high polarization conditions, also including variations in local pH, CO_2 availability, and surface coverage of reaction intermediates.

In this scenario, the better catalytic properties attained by the P-Sh_m sample is also demonstrated by the relatively less negative and more stable average potential values attained at each target current density, especially if compared to those exhibited by the H-TP_m electrode, originally composed by tabular-prismatic CuO particles (see Table S1).

Aiming at further highlighting the catalytic differences among the investigated CuO-based materials, the partial current densities of H_2, CO and C_2H_4 (indicated as J_{H2}, J_{CO} and J_{C2H4}) attained with the corresponding GDEs prepared with a medium catalyst loading can be directly compared in Fig. 4.

Firstly, the undesired hydrogen production, representing a serious parasite reaction because occurring at the expense of the FE for CO_2RR, resulted to proceed differently on the tested samples. In particular, while H-TP and PT-Sp catalysts exhibit a relatively high J_{H2}, with a sharp increase above the application of a total current density of 200 mA cm^{-2}, the most efficient P-Sh clearly minimizes hydrogen evolution, by keeping J_{H2} significantly below 40 mA cm^{-2} on the whole investigated total applied current density (see Fig. 4**a**).

Concerning the catalytic evolution of the two main CO_2-derived gaseous products, while J_{CO} tends to progressively slow down (Fig. 4**b**), J_{C2H4} almost linearly increases by applying a more negative total current density (Fig. 4**c**).

The observation that operating at more cathodic potential favors C–C coupling over C_1 products pathway agrees with literature and explains the systematic increase of FE_{C2H4}/FE_{CO} ratio attained with all the catalysts as the potential becomes more negative. Moreover, the complete absence of any partial current density for ethylene production upon the application of a total 50 mA cm^{-2} (unlike to what observed for the other gaseous products) demonstrates that the C–C coupling mechanism requires a minimum activation current. This threshold is necessary to drive the CO_2 reduction at a rate high enough to generate a proper accumulation of activated CO intermediates.

Further confirmation of the ability exhibited by the investigated materials in favoring the CO_2 conversion into C_{2+} species is obtained from liquid products analysis *via* ^{1}H NMR analysis, especially for the P-Sh sample. In fact, as reported in Table 3, a FE for ethanol of *ca.* 12%, together with traces of propanol (6%) and acetate (1%), has been attained in the electrochemical CO_2RR performed at 200 mA cm^{-2} with P-Sh_m sample. Lower overall FE towards liquid and gaseous C_{2+} species have been attained with both PT-Sp_m and H-TP_m samples.

Table 3
Faradaic Efficiencies for liquid products (formic acid, acetic acid, ethanol and propanol) collected during the CO_2 electrocatalytic reduction at 200 mA cm^{-2} with P-Sh_m, PT-Sp_m and H-TP_m samples. The uncertainty associated to the reported mean FE values resulted to be lower than 5%.

Liquid products	**FE at 200 mA cm^{-2} (%)**		
	P-Sh_m	PT-Sp_m	H-TP_m
Formic acid	4	5	4
Acetic acid	1	1	1
Ethanol	12	11	10
Propanol	6	4	2
Total	**23**	**22**	**17**

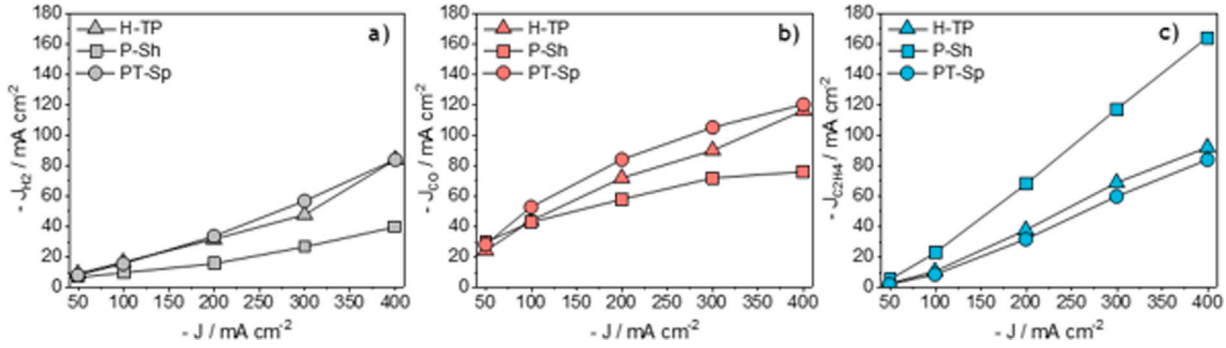

Fig. 4. Partial current density for a) H_2, b) CO and c) C_2H_4 production attained with H-TP_m (triangle symbols), P-Sh_m (square symbols) and PT-Sp_m (circle symbols) electrodes.

Importantly, this kind of analysis allowed to close the total FE balance to *ca.* 100%, verifying the effective production of other C_{2+} liquid hydrocarbons, thus excluding any significant underestimation of H_2, which may not be detected if it accumulates into the catholyte solution without being released in the gas phase compartment of the here adopted flow cell.

Furthermore, preliminary tests confirmed the excellent ability exclusively exhibited by the best performing P-Sh_m electrode in favoring the CO_2 reduction with a satisfying stability, guaranteeing the obtainment of almost unvaried FE towards C_2H_4 product (*ca.* 40–45%) up to 3 h of reaction at 400 mA cm^{-2} (see Figure S4 and Table S2). Differently, the catalytic performance of both PT-Sp_m and H-TP_m materials started to get worst relatively early, as demonstrated by the noisy potential signal registered few minutes after reaching the target 400 mA cm^{-2} current density (see Figure S4). This behavior may be ascribed to the structural reconstruction experienced by such materials, undergoing to severe aggregation (*vide* Section 3.4), leaving uncovered area of the underlying C paper, which may undermine the overall GDE stability, thus inducing the undesired flooding, that is the electrolyte permeation across the C paper, accompanied by H_2 production, as supported by the FE data attained during their stability tests and collected in Table S2**.**

3.3. FT-IR spectroscopy of adsorbed CO

Fourier Transform Infrared (FT-IR) spectroscopy using probe molecules was employed to perform a detailed surface characterization of the samples. The selected probe molecule was carbon monoxide (CO) since it is sensitive to the oxidation state and local environment of the Cu surface sites [84,85]. Before the spectroscopic measurements, the ECs were outgassed at 200 °C to remove the physisorbed water, thus allowing the adsorption of the CO probe molecules.

As shown in Fig. 5, the spectra of P-Sh are dominated by an intense band centered at 2110 cm^{-1}, accompanied by a higher-frequency shoulder at 2135 cm^{-1} and by a very weak component in the 2200–2190 cm^{-1} region, detectable mainly at the highest CO equilibrium pressure. For PT-Sp, by contrast, a much broader and less intense band envelope is observed, with a maximum at 2095 cm^{-1} and no clearly resolved high-frequency contributions. Finally, the extremely low specific surface area of the H-TP sample prevented the detection of signals from adsorbed CO.

The band positions suggest that the two materials expose different copper surface environments and comparison with single-crystal copper literature provides a useful frame of reference. On metallic Cu single crystal surfaces, the singleton C–O stretching frequency of linearly adsorbed CO falls in the range 2085–2075 cm^{-1} for well-coordinated terrace sites on the most stable Cu (111) and (100) surfaces [86]. The ν(CO) frequency is sensitive to the local coordination number of the adsorbing Cu atom: for instance, for the Cu (211) surface the signal is blueshifted to 2093 cm^{-1} for step sites and even to 2110 cm^{-1} for kink sites [87]. Also a partial or full oxidation of the Cu surface produces a blueshift of the signals which appear in the 2140–2110 cm^{-1} range [87]. Based on these literature results, the broad absorption centered at 2095 cm^{-1} in PT-Sp can be thus assigned to adsorption on metallic or partially reduced low-coordination Cu sites. While the main component observed for P-Sh at 2110 cm^{-1} lies at the upper edge of the range usually associated with metallic Cu and therefore is more safely interpreted as arising from cationic sites, like $Cu^{\delta+}$ or Cu^{+} [88,89].

The higher-frequency components observed for P-Sh further support the presence of cationic copper species. Literature on CO adsorption over Cu-containing materials and CuO-supported systems assigns bands in the *ca.* 2130 cm^{-1} range to Cu^{+}–CO monocarbonyls [88], whereas weak features between 2210 and 2180 cm^{-1} are characteristic of unstable Cu^{2+}–CO adducts, usually detectable only at low temperature and rapidly removed upon CO evacuation [90].

The spectroscopic results suggest that the investigated CuO morphologies do not simply differ in geometric shape, but also in the nature and distribution of accessible Cu surface sites. In particular, the larger contribution of cationic Cu species observed for P-Sh indicates a surface environment substantially different from that of PT-Sp. This observation, combined with the superior C_2H_4 selectivity exhibited by P-Sh, supports the hypothesis that the EC morphology influences the catalytic response through both geometric and electronic effects. Therefore, the enhanced e-CO_2RR performance of the sheet-like EC (*i.e.*, P-Sh) seems the result of a combined morphology–surface chemistry relationship rather than as a merely shape-only effect.

3.4. GDE characterization

After assembling the GDE via spray coating, their morphology was studied with SEM analysis at different magnifications to assess whether the shape of the starting powders was retained after the spray and to verify that an even, complete coverage of the C paper was achieved. To do so, electrodes with the highest loading were imaged for all

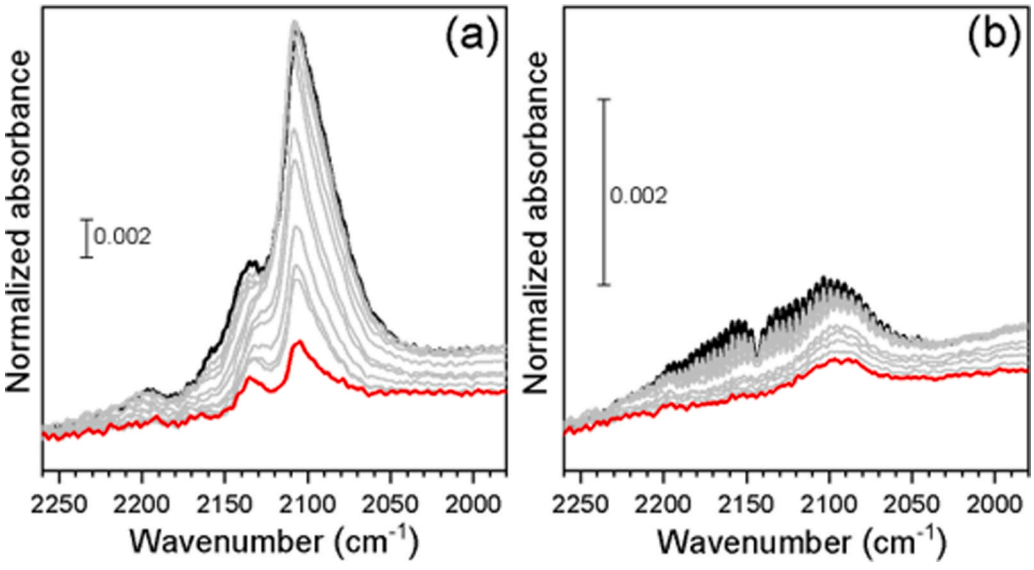

Fig. 5. FT-IR spectra of CO adsorbed at *ca.* 100 K at different coverages starting from 3 mbar (black curves) with stepwise outgassing till $5{\cdot}10^{-4}$ mbar (red curves) for samples a) P-Sh and b) PT-Sp. The spectrum of the sample before dosing CO was subtracted from all the spectra.

investigated samples (Fig. 6).

The shape of the H-TP sample is observable in Fig. 6**a-c**. Moreover, this loading was suitable to achieve satisfactory coverage of the underlying C paper, with only a few spots leaving it exposed. The highest-magnification image shows that Nafion wraps the nanoparticles with a continuous coating, which smooths the sharp edges observed in the SEM images of the pure nanoparticles (Fig. 2**a**).

On the other hand, the same loading of PT-Sp nanoparticles is unable to fully coat the C paper, which appears largely uncoated (Fig. 6**d-e**), with its pattern observable at the highest magnification (Fig. 6**f**). Therefore, the sheet-like nanoparticles cover the C paper more effectively due to their in-plane assembly, with the particles facing each other's largest crystal plane, thus resulting in a homogeneous and continuous layer. Conversely, the spherical particles retain the same tendency to agglomerate as observed in the original powder sample (Fig. 2**c-d**), thereby forming large clusters and leading to a heterogeneous coverage.

Leveraging the ability of the plate-like nanoparticles to stack on their largest facet, the P-Sh sample, due to its 2D sheet-like architecture, enables the complete coating of the C paper. Indeed, SEM images of the P-Sh GDE lack the typical features of the C paper (Figure S5, *SI*) at all the investigated magnifications (Fig. 6**g-i**).

SEM images of a GDE prepared with optimized medium P-Sh loading (Fig. 7**a, b**) show a full coverage of the underlying C paper, attesting to the excellent ability of this sample architecture to spread effectively thanks to its 2D shape.

Ex-post SEM images of the same P-Sh_m GDE indicate that the pristine catalyst undergoes severe reconstruction during the e-CO_2RR, as a consequence of the reduction of copper oxide under reaction conditions [91–93]. Indeed, after reaction, we can clearly appreciate that the initial micrometric-length sheets are composed of small, sphere-like nanoparticles with mean size of few nm, as predicted by XRD analysis (see Table 2), though P-Sh sample retain the original sheet-like structure network (Fig. 7**c**). The presence of a continuous nanoparticles network and the evidence that almost all sheets underwent this considerable change testify that all nanoparticles are electrically conductive during the CO_2 reduction and can participate in the reaction (Figures S6, *SI*). Interestingly, even after prolonged e-CO_2RR, the P-Sh_m electrode retained its sheet-like structural integrity (Figure S7, SI), thus guaranteeing stable catalytic performance, as previously detailed.

Differently, both PT-Sp_m and H-TP_m underwent significant modifications of their original spheroidal or tabular-prismatic particle shapes. In fact, ex-post SEM images of PT-Sp_m and H-TP_m GDEs clearly show that the applied electrochemical reductive conditions dramatically damage both their particles original structural integrity and distribution on the C paper (Figures S8-S9, *SI*). In both cases, the EC particles tend to coalesce up to the formation of a structureless layer of CuO-based material surrounded by uncovered areas of C paper, negatively affecting the overall e-CO_2RR efficiency.

For a more comprehensive characterization of the post-reaction electrodes, Raman spectroscopy measurements were performed. As shown in Fig. 8**a**, the Raman spectrum of the electrode before reaction clearly displays bands at 299, 346, and 631 cm^{-1}, which can be assigned to CuO vibrational modes, with symmetry A_g, B_g and B_g, respectively [94]. In contrast, in the spectrum of the post-reaction sample (Fig. 8**b**), different bands are observed at 150, 218, 415 and 640 cm^{-1}, indicating the formation of Cu_2O. It should be noted that, for ideal cubic cuprite Cu_2O, only the $T_{2\,g}$ mode is first-order Raman allowed, whereas several commonly observed bands arise from defect-induced activation of IR-active or silent modes, as well as from second-order Raman

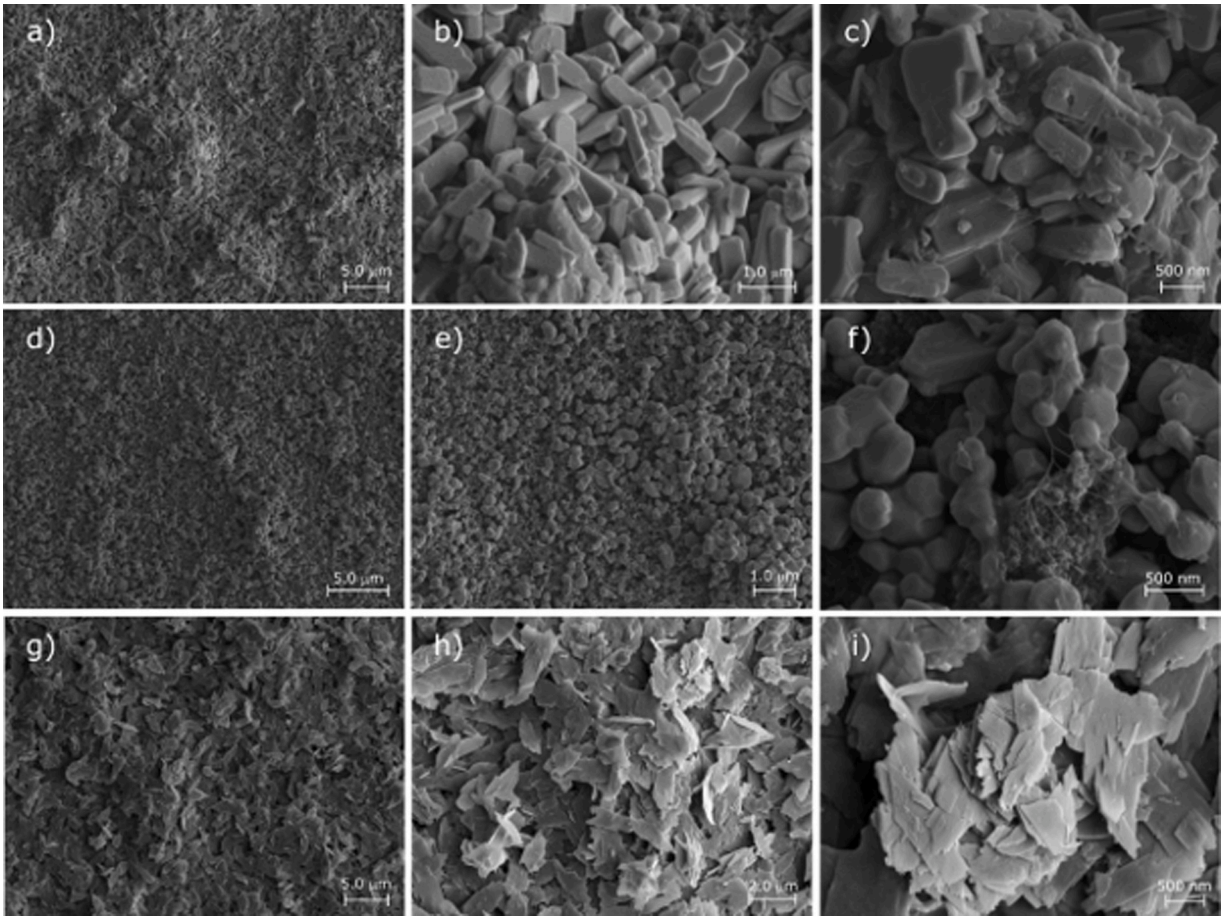

Fig. 6. SEM images of the (a-c) H-TP_h, (d-f) PT-Sp_h and (g-j) P-Sh_h GDEs at different magnifications with the corresponding scale bars.

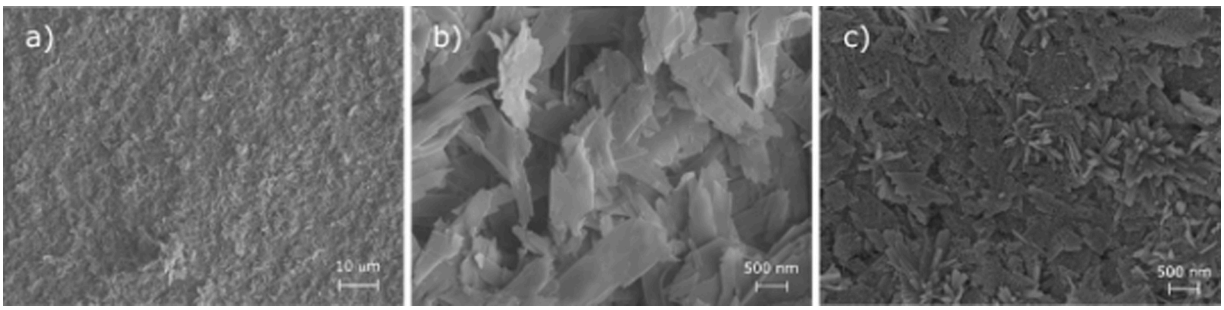

Fig. 7. SEM images of the P-Sh_m GDE (a-b) before and c) after performing the e-CO_2RR. The scale bars refer to adopted magnifications.

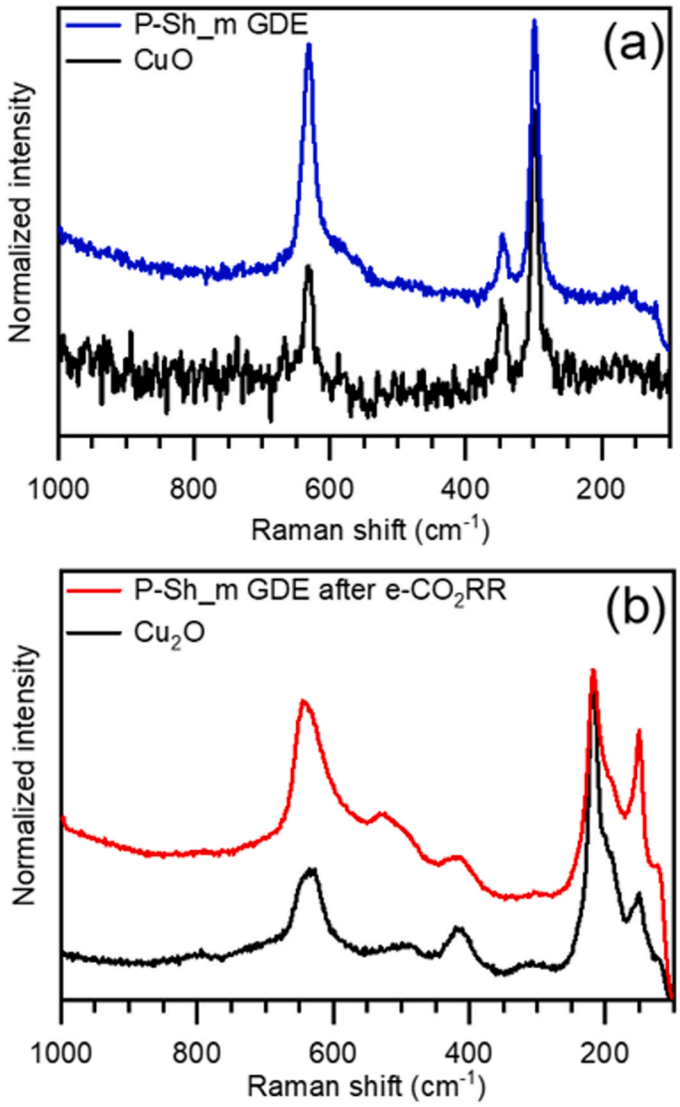

Fig. 8. Raman spectra of the P-Sh_m GDE (a) before and (b) after performing the e-CO_2RR, compared to commercial pure CuO and Cu_2O samples.

scattering. Accordingly, the band at 150 cm^{-1} can be attributed to a defect-activated T_{1u} mode, while the intense feature at around 218 cm^{-1} is commonly assigned to a second-order Raman mode of Cu_2O [95]. The bands at 415 cm^{-1} can be tentatively ascribed to a defect-activated Cu_2O mode, whereas the feature at 640 cm^{-1} is associated with high-frequency T_{1u} mode [96]. The appearance of these Cu_2O-related bands after e-CO_2RR indicates the formation of reduced copper oxide phases upon electrocatalysis. This modification in the Raman spectrum after reaction is fully consistent with the modifications observed by SEM and in agreement with previous studies reporting the formation of reduced Cu phases during electrocatalytic CO_2 reduction [91–93].

Taken together, these findings support that the high activity of P-Sh sample stems from its ability to form a continuous coating on the C paper, which provides abundant and proximal catalytically active sites, promoting the C–C coupling, resulting in a 52% FE for total C_{2+} products (gas and liquid) at 200 mA cm^{-2}, largely overperforming the other two samples (32% FE total C_{2+} products). However, the improved performance of the P-Sh EC cannot be solely attributed to its 2D morphology. In fact, morphology influences several EC properties simultaneously, including SSA, accessible Cu surface sites, EC layer homogeneity, and local mass-transport conditions. The complete coverage of the GDE achieved by the sheet-like system generates a highly interconnected catalytic network that should facilitate the accumulation of CO-derived intermediates and increase the probability of occurrence of C–C coupling reactions. Conversely, spheroidal and tabular-prismatic systems form less homogeneous EC layers and expose a lower density of accessible Cu active sites, resulting in a minor CO_2RR C_2-selectivity and an enhanced HER. These observations indicate that the initial morphology affects the catalytic performance through its impact on the EC architecture and local reaction environment rather than through a purely geometric effect.

4. Conclusions

Three CuO materials with different morphology were synthesized and tested as electrocatalysts for CO_2RR. Despite sharing the same bulk CuO crystal phase, the samples exhibited marked differences in crystallite size, specific surface area, exposed surface sites, and catalyst-layer organization on the GDE, which strongly affected their catalytic behavior.

The sheet-like P-Sh sample displayed the highest specific surface area and the best overall performance, combining high selectivity toward C_2 products and effective suppression of HER. FT-IR spectroscopy of adsorbed CO indicate that P-Sh exposes a larger amount of spectroscopically distinct adsorption sites, including Cu^+ and a minor fraction of Cu^{2+} centers, whereas PT-Sp is characterized by a heterogeneous distribution of more metallic Cu environments. Moreover, SEM analysis of the GDEs revealed that the 2D sheet-like architecture of P-Sh enables a more homogeneous catalyst coating, likely leading to a higher density of proximal active sites, which favors the formation of multi-carbon products.

Overall, this work demonstrates that the electrocatalytic behavior of oxide-derived Cu ECs is governed by a complex interplay between morphology, surface chemistry, and EC layer architecture. Although the sheet-like P-Sh system exhibited the highest selectivity toward C_2 products, the present study reveals that this behavior cannot be explained solely by its 2D morphology. Instead, the improved performance originates from the simultaneous presence of a higher accessible surface area, distinct Cu surface environments identified by FT-IR

spectroscopy, and the formation of a homogeneous EC coating on the gas diffusion electrode that facilitates the generation and coupling of reaction intermediates.

Furthermore, this study also demonstrated that in the case of sheet-like system, the initial CuO morphology is retained even after prolonged e-CO_2RR operating conditions, generating a highly interconnected catalytic network that promotes C–C coupling reactions enhancing the formation of C_2 products. Vice versa, both tabular-prismatic and spheroidal systems gave an important structural reconstruction, thus leading to a less favorable EC layer organization and lower e-CO_2RR selectivity.

These findings provide a comprehensive correlation on the structure–property performance of oxide-derived Cu ECs and offer practical guidelines for the rational design of Cu-based ECs employable in e-CO_2RR processes.

CRediT authorship contribution statement

Rodriguez-Flores Tatiana: Writing – review & editing, Investigation, Formal analysis. **Davide Melotto:** Writing – review & editing, Investigation, Formal analysis. **Laura Vigni:** Investigation, Formal analysis, Data curation. **Falak Shafiq:** Writing – review & editing, Writing – original draft, Investigation, Formal analysis. **Roberto Nisticò:** Writing – review & editing, Writing – original draft, Supervision, Resources, Investigation, Formal analysis, Conceptualization. **Maria Vittoria Dozzi:** Writing – review & editing, Writing – original draft, Supervision, Resources, Investigation, Formal analysis, Conceptualization. **Lorenzo Mino:** Writing – review & editing, Writing – original draft, Supervision, Resources, Investigation, Formal analysis, Conceptualization. **Ivan Grigioni:** Writing – review & editing, Writing – original draft, Supervision, Investigation. **Elizaveta Kozyr:** Writing – review & editing, Investigation, Formal analysis.

Declaration of Competing Interest

The authors declare that they have no known competing financial interests or personal relationships that could have appeared to influence the work reported in this paper.

Acknowledgements

This work received financial support from MUR (Italy) and the European Union – Next Generation EU, Mission 4, Component 1, CUP (H53D23004490001) through the PRIN Project MAPEC (N. 2022599NR3), and CUP (H53D23008000001) through the PRIN Project PERFECT (N. P2022TK9B9), which are gratefully acknowledged. This work has been funded within the framework of the Regional Programme of the European Regional Development Fund 2021–2027 of Regione Lombardia (PR FESR 2021–2027, Action 1.1.3, in compliance with European Regulation No. 1060/2021), following the public call "Collabora&Innova". Project "CO_2: from a global problem to a tool to implement circularity – CO-Tool" (Project ID 6144755). L.M. acknowledges support from the Project CH4.0 under the MUR program "Dipartimenti di Eccellenza 2023–2027" (CUP: D13C22003520001). Unitech COSPECT Transmission Electron Microscope facility and Unitech NOLIMITS at Università degli Studi di Milano are gratefully acknowledged. Authors would like to acknowledge Dr. Paolo Gentile (University of Milano-Bicocca, Italy) for the technical support during the SEM analysis on the ECs and Alessio Cambiaghi (University of Milan) for the EC experiments performed during the revision process. Alessandro Damin and Natale Gabriele Porcaro (University of Torino) are gratefully acknowledged for the support in the Raman analysis.

Appendix A. Supporting information

Supplementary data associated with this article can be found in the online version at doi:10.1016/j.mtcata.2026.100147.

Data availability

Data will be made available on request.

References

[1] G. Zang, P. Sun, A. Elgowainy, M. Wang, Technoeconomic and life cycle analysis of synthetic methanol production from hydrogen and industrial byproduct CO_2, Environ. Sci. Technol. 55 (2021) 5248–5257, https://doi.org/10.1021/acs.est.0c08237.

[2] A. Haruna, G. Tanimu, I. Ibrahim, Z.N. Garba, S.M. Yahaya, S.G. Musa, Z.M. A. Merican, Mitigating oil and gas pollutants for a sustainable environment – critical review and prospects, J. Clean. Prod. 416 (2023) 137863, https://doi.org/10.1016/j.jclepro.2023.137863.

[3] J. Bebbington, T. Schneider, L. Stevenson, A. Fox, Fossil fuel reserves and resources reporting and unburnable carbon: investigating conflicting accounts, Crit. Perspect. Account. 66 (2020) 102083, https://doi.org/10.1016/j.cpa.2019.04.004.

[4] H. Karunathilake, S. Witharana, Fossil Fuels and Global Energy Economics, in: M. R. Rahimpour (Ed.), in: Encyclopedia of Renewable Energy, Sustainability and the Environment (First Edition), Elsevier: Oxford (UK, 2024, pp. 107–120, https://doi.org/10.1016/B978-0-323-93940-9.00050-5.

[5] A.T. Ubando, A.J.R. Del Rosario, W.-H. Chen, A.B. Culaba, A state-of-the-art review of biowaste biorefinery, Environ. Pollut. 269 (2021) 116149, https://doi.org/10.1016/j.envpol.2020.116149.

[6] R. Chandra, H.M.N. Iqbal, G. Vishal, H.-S. Lee, S. Nagra, Algal biorefinery: a sustainable approach to valorize algal-based biomass towards multiple product recovery, Bioresour. Technol. 278 (2019) 346–359, https://doi.org/10.1016/j.biortech.2019.01.104.

[7] R. Kumari, M. Kumar, V. Vivekanand, N. Pareek, Chitin biorefinery: a narrative and prophecy of crustacean shell waste sustainable transformation into bioactives and renewable energy, Renew. Sustain. Energy Rev. 184 (2023) 113595, https://doi.org/10.1016/j.rser.2023.113595.

[8] E. Montoneri, M. Koutinas, E. Padoan, V. Negro, C. Licignano, S. Leone, P. Photiou, M. Kallis, I. Vyrides, F. Liendo, M. Negre, S. Solaro, M. Antonini, D. Mainero, A. Vlysidis, V. Konstantinidis, D. Ladakis, S. Maina, A. Koutinas, Integrated chemical and biochemical technology to produce biogas with a reduced ammonia content from municipal biowaste. Validating lab-scale research in a real operational environment, Environ. Sci.: Adv. 1 (2022) 746–768, https://doi.org/10.1039/D2VA00068G.

[9] S. Tabasso, M. Ginepro, L. Tomasso, E. Montoneri, R. Nisticò, M. Francavilla, Integrated biochemical and chemical processing of municipal bio-waste to obtain bio based products for multiple uses. The case of soil remediation, J. Clean. Prod. 245 (2020) 119191, https://doi.org/10.1016/j.jclepro.2019.119191.

[10] J. Wang, C.-S. Jia, C.-J. Li, X.-L. Peng, L.-H. Zhang, J.-Y. Liu, Thermodynamic properties for carbon dioxide, ACS Omega 4 (2019) 19193–19198, https://doi.org/10.1021/acsomega.9b02488.

[11] D.D. Zhu, J.L. Liu, S.Z. Qiao, Recent advances in inorganic heterogeneous electrocatalysts for reduction of carbon dioxide, Adv. Mater. 28 (2016) 3423–3452, https://doi.org/10.1002/adma.201504766.

[12] L.K. Putri, B.-J. Ng, W.-J. Ong, S.-P. Chai, A.R. Mohamed, Toward excellence in photocathode engineering for photoelectrochemical CO_2 reduction: design rationales and current progress, Adv. Energy Mater. 12 (2022) 2201093, https://doi.org/10.1002/aenm.202201093.

[13] P. Intarapong, S. Yongprapat, R. Saelim, S. Therdthianwong, M. Nithitanakul, A. Therdthianwong, Recycling copper wire waste into active Cu-based catalysts for value-added chemicals production via CO_2 electrochemical reduction, J. Ind. Eng. Chem. 145 (2025) 773–782, https://doi.org/10.1016/j.jiec.2024.10.074.

[14] Q. Yang, C.-C. Yang, C.-H. Lin, H.-L. Jiang, Metal–organic-framework-derived hollow N-doped porous carbon with ultrahigh concentrations of single Zn atoms for efficient carbon dioxide conversion, Angew. Chem. Int. Ed. 58 (2019) 3511–3515, https://doi.org/10.1002/anie.201813494.

[15] B. Han, X. Ou, Z. Deng, Y. Song, C. Tian, H. Deng, Y.-J. Xu, Z. Lin, Nickel metal–organic framework monolayers for photoreduction of diluted CO_2: metal-node-dependent activity and selectivity, Angew. Chem. Int. Ed. 130 (2018) 17053–17057, https://doi.org/10.1002/ange.201811545.

[16] P. Dessì, L. Rovira-Alsina, C. Sanchez, G.K. Dinesh, W. Tong, P. Chatterjee, M. Tedesco, P. Farras, H.M.V. Hamelers, S. Puig, Microbial electrosynthesis: towards sustainable biorefineries for production of green chemicals from CO_2 emissions, Biotechnol. Adv. 46 (2021) 107675, https://doi.org/10.1016/j.biotechadv.2020.107675.

[17] C. Zhan, F. Dattila, C. Rottenmaier, A. Herzog, M. Herran, T. Wagner, F. Scolten, A. Bergmann, N. Lopez, B.R. Cuenya, Key intermediates and Cu active sites for CO_2 electroreduction to ethylene and ethanol, Nat. Energy 9 (2024) 1485–1496, https://doi.org/10.1038/s41560-024-01633-4.

[18] J. Han, X. Bai, X. Xu, X. Bai, A. Husile, S. Zhang, L. Qi, J. Guan, Advances and challenges in the electrochemical reduction of carbon dioxide, Chem. Sci. 15 (2024) 7870–7907, https://doi.org/10.1039/D4SC01931H.

[19] S.A. Al-Tamreh, M.H. Ibrahim, M.H. El-Naas, J. Vaes, D. Pant, A. Benamor, A. Amhamed, Electroreduction of carbon dioxide into formate: a comprehensive review, ChemElectroChem 8 (2021) 3207–3220, https://doi.org/10.1002/celc.202100438.

[20] A.R. Woldu, Z. Huang, P. Zhao, L. Hu, D. Astruc, Electrochemical CO_2 reduction (CO_2RR) to multi-carbon products over copper-based catalysts, Coord. Chem. Rev. 454 (2022) 214340, https://doi.org/10.1016/j.ccr.2021.214340.

[21] J. Kim, S. Jeong, M. Beak, J. Park, K. Kwon, Performance of photovoltaic-driven electrochemical cell systems for CO_2 reduction, Chem. Eng. J. 428 (2022) 130259, https://doi.org/10.1016/j.cej.2021.130259.

[22] D. Xu, K. Li, B. Jia, W. Sun, W. Zhang, X. Liu, T. Ma, Electrocatalytic CO_2 reduction towards industrial applications, Carbon Energy 5 (2023) e230, https://doi.org/10.1002/cey2.230.

[23] X. Zhao, K. Zhao, Y. Liu, Y. Su, S. Chen, H. Yu, X. Quan, Highly efficient electrochemical CO_2 reduction on a precise homonuclear diatomic Fe–Fe catalyst, ACS Catal. 12 (2022) 11412–11420, https://doi.org/10.1021/acscatal.2c03149.

[24] Y. Zhao, H. Li, X. Wang, T. Cong, Y. Wang, H. Zheng, Z. Zhao, X. Feng, J. Feng, P. Wang, K. Yang, X. Ding, Highly stable and efficient catalyst fabricated with in situ exsolved Co-Fe bimetallic nanoparticles anchored on $(Ba_{0.9}K_{0.1})_{0.9}Co_{0.5}Fe_{0.4}Nb_{0.1}O_{3-\delta}$ for CO_2 electrolysis, Mater. Sci. Eng. B 321 (2025) 118458, https://doi.org/10.1016/j.mseb.2025.118458.

[25] W. Yang, Z. Xue, J. Yang, J. Xian, Q. Liu, Y. Fan, K. Zheng, P. Liao, H. Su, Q. Liu, G. Li, C.-Y. Su, Fe nanoparticles embedded in N-doped porous carbon for enhanced electrocatalytic CO_2 reduction and Zn-CO_2 battery, Chin. J. Catal. 48 (2023) 185–194, https://doi.org/10.1016/S1872-2067(23)64415-8.

[26] X. Liu, Y. Hou, F. Yang, Y. Liu, H. Yu, X. Han, J. Chen, S. Chen, S. Zhou, S. Deng, J. Wang, Selective CO_2 electroreduction to ethanol on encapsulated nickel nanoparticles by N-doped carbon nanotubes, Carbon 201 (2023) 460–466, https://doi.org/10.1016/j.carbon.2022.09.010.

[27] Y. Zhang, P. Li, C. Zhao, G. Zhou, F. Zhou, Q. Zhang, Multicarbons generation factory: CuO/Ni single atoms tandem catalyst for boosting the productivity of CO_2 electrocatalysis, Sci. Bull. 67 (2022) 1679–1687, https://doi.org/10.1016/j.scib.2022.07.029.

[28] A.R. Haines, J.C. Hemminger, Stability of Cu/TiO_2 nanoparticle model catalysts under electrochemical CO_2 reduction conditions, ACS Catal. 11 (2021) 6960–6970, https://doi.org/10.1021/acscatal.1c01955.

[29] S. Gul, F. Nasim, M.A. Nadeem, M. Imran, A. Wasem, M.A. Nadeem, Effective electrocatalytic conversion of CO_2 to CO on CoO-NC supported iron oxide heterostructure, Electrochim. Acta 514 (2025) 145575, https://doi.org/10.1016/j.electacta.2024.145575.

[30] M. Umar, M.Y. Aljezan, I. Abdulazeez, A.O. Amao, S.A. Ganiyu, K. Alhooshani, Modulating the electrocatalytic reduction of CO_2 to CO via surface reconstruction of ZnO nanoshapes, J. Sci. Adv. Mater. Devices 9 (2024) 100748, https://doi.org/10.1016/j.jsamd.2024.100748.

[31] T. Wang, X. Duan, R. Bai, H. Li, C. Qin, J. Zhang, Z. Duan, K.-J. Chen, F. Pan, Ni-electrocatalytic CO_2 reduction toward ethanol, Adv. Mater. 36 (2024) 2410125, https://doi.org/10.1002/adma.202410125.

[32] L. Fang, X. Lyu, J.J. Xu, Y. Liu, X. Hu, B.J. Reinhart, T. Li, Operando X-ray absorption spectroscopy study of SnO_2 nanoparticles for electrochemical reduction of CO_2 to formate, ACS Appl. Mater. Interfaces 14 (2022) 55636–55643, https://doi.org/10.1021/acsami.2c17481.

[33] S.S.A. Shah, M.S. Javed, T. Najam, C. Malochas, N.A. Khan, M.A. Nazir, M. Xu, P. Tsiakaras, S.-J. Bao, Metal oxides for the electrocatalytic reduction of carbon dioxide: mechanism of active sites, composites, interface and defect engineering strategies, Coord. Chem. Rev. 471 (2022) 214716, https://doi.org/10.1016/j.ccr.2022.214716.

[34] W. Zhang, C. Huang, Q. Xiao, L. Yu, L. Shuai, P. An, J. Zhang, M. Qiu, Z. Ren, Y. Yu, Atypical oxygen-bearing copper boosts ethylene selectivity toward electrocatalytic CO_2 reduction, J. Am. Chem. Soc. 142 (2020) 11417–11427, https://doi.org/10.1021/jacs.0c01562.

[35] M. Abdinejad, Z. Mirza, X. Zhang, H.-B. Kraatz, Enhanced electrocatalytic activity of primary amines for CO_2 reduction using copper electrodes in aqueous solution, ACS Sustain. Chem. & Eng. 8 (2020) 1715–1720, https://doi.org/10.1021/acssuschemeng.9b06837.

[36] P. Devi, K. Malik, E. Arora, S. Bhattacharya, V. Kalendra, K.V. Lakshmi, A. Verma, J.P. Singh, Selective electrochemical reduction of CO_2 to CO on CuO/In_2O_3 nanocomposites: Role of oxygen vacancies, Catal. Sci. Technol. 9 (2019) 5339–5349, https://doi.org/10.1039/C9CY01396B.

[37] M. He, X. Chang, T.-H. Chao, C. Li, W.A. Goddard III, M.-J. Cheng, B. Xu, Q. Lu, Selective enhancement of methane formation in electrochemical CO_2 reduction enabled by a Raman-inactive oxygen-containing species on Cu, ACS Catal. 12 (2022) 6036–6046, https://doi.org/10.1021/acscatal.2c00087.

[38] X. Chen, T. Zhao, J. Han, Y. Bu, Copper-based catalysts for electrochemical reduction of carbon dioxide to ethylene, ChemPlusChem 88 (2023) e202200370, https://doi.org/10.1002/cplu.202200370.

[39] S.Y. Lee, H. Jung, N.-K. Kim, H.-S. Oh, B.K. Min, Y.J. Hwang, Mixed copper states in anodized Cu electrocatalyst for stable and selective ethylene production from CO_2 reduction, J. Am. Chem. Soc. 140 (2018) 8681–8689, https://doi.org/10.1021/jacs.8b02173.

[40] V.S. Saji, Nanotubes-nanosheets (1D/2D) heterostructured bifunctional electrocatalysts for overall water splitting, Electrochim. Acta 430 (2022) 141095, https://doi.org/10.1016/j.electacta.2022.141095.

[41] T.-T. Zhuang, Y. Peng, Z.-Q. Liang, Z. Wang, Y. Li, C.-S. Tan, J. Li, C.T. Dinh, P. De Luca, P.-L. Hsieh, T. Burdyny, H.-H. Li, M. Liu, Y. Wang, F. LI, A. Proppe, A. Johnston, D.-H. Nam, Z.-Y. Wu, Y.-R. Zheng, A.H. Ip, H. Tan, L.-J. Chen, S.-H. Yu, S.O. Kelly, D. Sinton, E.H. Sargent, Copper nanocavities confine intermediates for efficient electrosynthesis of C3 alcohol fuels from carbon monoxide, Nat. Catal. 1 (2018) 946–951, https://doi.org/10.1038/s41929-018-0168-4.

[42] A.H.M. da Silva, S.J. Raaijman, C.S. Santana, J.M. Assaf, J.F. Gomes, M.T.M. Koper, Electrocatalytic CO_2 reduction to C_{2+} products on Cu and Cu_xZn_y electrodes: effects of chemical composition and surface morphology, J. Electroanal. Chem. 880 (2021) 114750, https://doi.org/10.1016/j.jelechem.2020.114750.

[43] I. Merino-Garcia, J. Albo, A. Irabien, Tailoring gas-phase CO_2 electroreduction selectivity to hydrocarbons at Cu nanoparticles, Nanotechnology 29 (2017) 014001, https://doi.org/10.1088/1361-6528/aa994e.

[44] E. Ruiz-López, J. Gandara-Loe, F. Baena-Morena, T.R. Reina, J.A. Odriozola, Electrocatalytic CO_2 conversion to C_2 products: catalysts design, market perspectives and techno-economic aspects, Renew. Sustain. Energy Rev. 161 (2022) 112329, https://doi.org/10.1016/j.rser.2022.112329.

[45] Y. Li, F. Cui, M.B. Ross, D. Kim, Y. Sun, P. Yang, Structure-sensitive CO_2 electroreduction to hydrocarbons on ultrathin 5-fold twinned copper nanowires. Nano Lett. 17 (2017) 1312–1317, https://doi.org/10.1021/acs.nanolett.6b05287.

[46] M. Favaro, H. Xiao, T. Cheng, W.A. Goddard III, J. Yano, E.J. Crumlin, Subsurface oxide plays a critical role in CO_2 activation by Cu(111) surfaces to form chemisorbed CO_2, the first step in reduction of CO_2, Proc. Natl. Acad. Sci. 114 (2017) 6706–6711, https://doi.org/10.1073/pnas.1701405114.

[47] J.L. Inglis, B.J. MacLean, M.T. Pryce, J.G. Vos, Electrocatalytic pathways towards sustainable fuel production from water and CO_2, Coord. Chem. Rev. 256 (2012) 2571–2600, https://doi.org/10.1016/j.ccr.2012.05.002.

[48] H.-R. Jhong, S. Ma, P.J.A. Kenis, Electrochemical conversion of CO_2 to useful chemicals: current status, remaining challenges, and future opportunities, Curr. Opin. Chem. Eng. 2 (2013) 191–199, https://doi.org/10.1016/j.coche.2013.03.005.

[49] C. Xiao, J. Zhang, Architectural design for enhanced C_2 product selectivity in electrochemical CO_2 reduction using Cu-based catalysts: a review, ACS Nano 15 (2021) 7975–8000, https://doi.org/10.1021/acsnano.0c10697.

[50] F. Chang, M. Xiao, R. Miao, Y. Liu, M. Ren, Z. Jia, D. Han, Y. Yuan, Z. Bai, L. Yang, Copper-based catalysts for electrochemical carbon dioxide reduction to multicarbon products, Electrochem. Energy Rev. 5 (2022) 4, https://doi.org/10.1007/s41918-022-00139-5.

[51] K. Wiranarongkorn, K. Eamsiri, Y.-S. Chen, A. Arpornwichanop, A comprehensive review of electrochemical reduction of CO_2 to methanol: technical and design aspects, J. CO_2 Util. 71 (2023) 102477, https://doi.org/10.1016/j.jcou.2023.102477.

[52] R. Lu, Y. Liu, Z. Wang, Advances in the understanding of selective CO_2 reduction catalysis, EcoEnergy 2 (2024) 695–713, https://doi.org/10.1002/ece2.67.

[53] J. Choi, H. Lim, S. Surendran, S. Park, J. Shim, G.H. Jeong, U. Sim, Harnessing electrochemical CO_2 reduction and assisted water electrolysis via constrained thermodynamic modeling, Phys. Chem. Chem. Phys. 27 (2025) 17198–17211, https://doi.org/10.1039/D5CP01408E.

[54] K.P. Kuhl, E.R. Cave, D.N. Abram, T.F. Jaramillo, New insights into the electrochemical reduction of carbon dioxide on metallic copper surfaces, Energy Environ. Sci. 5 (2012) 7050–7059, https://doi.org/10.1039/C2EE21234J.

[55] R.M. Arán-Ais, F. Scholten, S. Kunze, R. Rizo, B.R. Cuenya, The role of in situ generated morphological motifs and Cu(I) species in C_{2+} product selectivity during CO_2 pulsed electroreduction, Nat. Energy 5 (2020) 317–325, https://doi.org/10.1038/s41560-020-0594-9.

[56] Y. Lum, J.W. Ager, Evidence for product-specific active sites on oxide-derived Cu catalysts for electrochemical CO_2 reduction, Nat. Catal. 2 (2019) 86–93, https://doi.org/10.1038/s41929-018-0201-7.

[57] D. Ren, Y. Deng, A.D. Handoko, C.S. Chen, S. Malkhandi, B.S. Yeo, Selective electrochemical reduction of carbon dioxide to ethylene and ethanol on copper (I) oxide catalysts, ACS Catal. 5 (2015) 2814–2821, https://doi.org/10.1021/cs502128q.

[58] H. Mistry, A.S. Varela, C.S. Bonifacio, I. Zegkinoglou, I. Sinev, Y.-W. Choi, Highly selective plasma-activated copper catalysts for carbon dioxide reduction to ethylene, Nat. Commun. 7 (2016) 12123, https://doi.org/10.1038/ncomms12123.

[59] H. Xiao, W.A. Goddard, T. Cheng, Y. Liu, Cu metal embedded in oxidized matrix catalyst to promote CO_2 activation and CO dimerization for electrochemical reduction of CO_2, Proc. Natl. Acad. Sci. 114 (2017) 6685–6688, https://doi.org/10.1073/pnas.1702405114.

[60] P. De Luna, R. Quintero-Bermudez, C.T. Dinh, M.B. Ross, O.S. Bushuyev, P. Todorovic, Catalyst electro-redeposition controls morphology and oxidation state for selective carbon dioxide reduction, Nat. Catal. 1 (2018) 103–110, https://doi.org/10.1038/s41929-017-0018-9.

[61] Y. Hori, I. Takahashi, O. Koga, N. Hoshi, Selective formation of C_2 compounds from electrochemical reduction of CO_2 at a series of copper single crystal electrodes, J. Phys. Chem. B 106 (2002) 15–17, https://doi.org/10.1021/jp013478d.

[62] Z.Z. Wu, X.L. Zhang, Z.Z. Niu, F.Y. Gao, P.P. Yang, L.P. Chi, Identification of Cu (100)/Cu(111) interfaces as superior active sites for CO dimerization during CO_2 electroreduction, J. Am. Chem. Soc. 144 (2022) 259–269, https://doi.org/10.1021/jacs.1c09508.

[63] K. Jiang, R.B. Sandberg, A.J. Akey, X. Liu, D.C. Bell, J.K. Nørskov, Metal ion cycling of Cu foil for selective C-C coupling in electrochemical CO_2 reduction, Nat. Catal. 1 (2018) 111–119, https://doi.org/10.1038/s41929-017-0009-x.

[64] F. Scholten, K.L. Nguyen, J.P. Bruce, M. Heyde, B. Roldan Cuenya, Identifying structure-selectivity correlations in the electrochemical reduction of CO_2: a comparison of well-ordered atomically clean and chemically etched copper single-crystal surfaces, Angew. Chem. Int. Ed. 60 (2021) 19169–19175, https://doi.org/10.1002/anie.202103102.

[65] M. Ma, K. Djanashvili, W.A. Smith, Controllable hydrocarbon formation from the electrochemical reduction of CO_2 over Cu nanowire arrays, Angew. Chem. Int. Ed. 55 (2016) 6680–6684, https://doi.org/10.1002/anie.201601282.

[66] A. Loiudice, P. Lobaccaro, E.A. Kamali, T. Thao, B.H. Huang, J.W. Ager, Tailoring copper nanocrystals towards C_2 products in electrochemical CO_2 reduction, Angew. Chem. Int. Ed. 55 (2016) 5789–5792, https://doi.org/10.1002/anie.201601582.

[67] A. Dutta, M. Rahaman, N.C. Luedi, M. Mohos, P. Broekmann, Morphology matters: tuning the product distribution of CO_2 electroreduction on oxide-derived Cu foam catalysts, ACS Catal. 6 (2016) 3804–3814, https://doi.org/10.1021/acscatal.6b00770.

[68] R. Priyadharsini, Shyamal Das, M. Venkateshwarlu, K. Deenadayalan, C. Manoharan, The influence of reaction and annealing temperature on physical and magnetic properties of $CuFe_2O_4$ nanoparticles: Hydrothermal method, Inorg. Chem. Communun. 140 (2022) 109406, https://doi.org/10.1016/j.inoche.2022.109406.

[69] D.P. Singh, A.K. Ojha, O.N. Srivastava, Synthesis of different $Cu(OH)_2$ and CuO (nanowires, rectangles, seed-, belt-, and sheetlike) nanostructures by simple wet chemical route, J. Phys. Chem. C. 113 (2009) 3409–3418, https://doi.org/10.1021/jp804832g.

[70] A.S. Ethiraj, D.J. Kang, Synthesis and characterization of CuO nanowires by a simple wet chemical method, Nanoscale Res. Lett. 7 (2012) 70, https://doi.org/10.1186/1556-276X-7-70.

[71] J. Ni, L. Jianfei, Z. Wang, The ultrahigh adsorption capacity and excellent photocatalytic degradation activity of mesoporous CuO with novel architecture, Nanomaterials 13 (2022) 142, https://doi.org/10.3390/nano13010142.

[72] Y.B. Chan, V. Selvanathan, L.-H. Tey, M. Akhtaruzzaman, F.H. Anur, S. Djearamane, A. Watanabe, M. Aminuzzaman, Effect of calcination temperature on structural, morphological and optical properties of copper oxide nanostructures derived from *Garcinia mangostana* l. leaf extract, Nanomaterials 12 (2022) 3589, https://doi.org/10.3390/nano12203589.

[73] R. Nisticò, A synthetic guide toward the tailored production of magnetic iron oxide nanoparticles, Bol. Soc. Esp. Ceram. Vidr. 60 (2021) 29–40, https://doi.org/10.1016/j.bsecv.2020.01.011.

[74] J.E. Pander III, D. Ren, Y. Huang, N.W.X. Loo, S.H.L. Hong, B.S. Yeo, Understanding the heterogeneous electrocatalytic reduction of carbon dioxide on oxide-derived catalysts, ChemElectroChem 5 (2018) 219–237, https://doi.org/10.1002/celc.201701100.

[75] A.M. Asiri, J. Gao, S.B. Khan, K.A. Alamry, H.M. Marwani, M.S.J. Khan, W. A. Adeosun, S.M. Zakeeruddin, D. Ren, M. Gratzel, Revisiting the impact of morphology and oxidation state of Cu on CO_2 reduction using electrochemical flow cell, J. Phys. Chem. Lett. 13 (2022) 345–351, https://doi.org/10.1021/acs.jpclett.1c03957.

[76] M. Jun, J. Kundu, D.H. Kim, M. Kim, D. Kim, K. Lee, S.-I. Choi, Strategies to modulate the copper oxidation state toward selective C_{2+} production in the electrochemical CO_2 reduction reaction, Adv. Mater. 36 (2024) 2313028, https://doi.org/10.1002/adma.202313028.

[77] H. Rabiee, L. Ge, X. Zhang, S. Hu, M. Li, Z. Yuan, Gas diffusion electrodes (GDEs) for electrochemical reduction of carbon dioxide, carbon monoxide, and dinitrogen to value-added products: a review, Energy Environ. Sci. 14 (2021) 1959–2008, https://doi.org/10.1039/D0EE03756G.

[78] V.G. Agarwal, S. Haussener, Quantifying mass transport limitations in a microfluidic CO2 electrolyzer with a gas diffusion cathode, Commun. Chem. 7 (2024) 47, https://doi.org/10.1038/s42004-024-01122-5.

[79] N. Zhang, Y. Zhang, Recent advances in electrocatalytic conversion of CO_2-to-ethylene: From reaction mechanisms to tuning strategies, Appl. Catal. B Environ. Energy 363 (2025) 124822, https://doi.org/10.1016/j.apcatb.2024.124822.

[80] G.L. De Gregorio, T. Burdyny, A. Loiudice, P. Iyengar, W.A. Smith, R. Buonsanti, Facet-dependent selectivity of Cu catalysts in electrochemical CO_2 reduction at commercially viable current densities, ACS Catal. 10 (2020) 4854–4862, https://doi.org/10.1021/acscatal.0c00297.

[81] K.J.P. Schouten, E. Pérez Gallent, M.T.M. Koper, The influence of pH on the reduction of CO and CO_2 to hydrocarbons on copper electrodes, J. Electroanal. Chem. 716 (2014) 53–57, https://doi.org/10.1016/j.jelechem.2013.08.033.

[82] H. Xiao, T. Cheng, W.A. Goddard III, R. W, Sundararaman, Mechanistic explanation of the pH dependence and onset potentials for hydrocarbon products from electrochemical reduction of CO on Cu (111), J. Am. Chem. Soc. 138 (2016) 483–486, https://doi.org/10.1021/jacs.5b11390.

[83] A.S. Varela, M. Kroschel, T. Reier, P. Strasser, Controlling the selectivity of CO_2 electroreduction on copper: the effect of the electrolyte concentration and the importance of the local pH, Catal. Today 260 (2016) 8–13, https://doi.org/10.1016/j.cattod.2015.06.009.

[84] S. Pantaleone, F. Pellegrino, V. Maurino, M. Corno, P. Ugliengo, L. Mino, Disclosing the true atomic structure of {001} facets in shape-engineered TiO_2 anatase nanoparticles, J. Mater. Chem. A 12 (2024) 4325–4332, https://doi.org/10.1039/D3TA06694K.

[85] G. Escolano-Casado, P. Ivanchenko, G. Paul, C. Bisio, L. Marchese, A.M. Ashrafi, V. Milosavljevic, L. Degli Esposti, M. Iafisco, L. Mino, Surface and structural characterization of Cu-exchanged hydroxyapatites and their application in H_2O_2 electrocatalytic reduction, Appl. Surf. Sci. 595 (2022) 153495, https://doi.org/10.1016/j.apsusc.2022.153495.

[86] D. Zhang, C. Jansen, O.T. Berg, J.M. Bakker, J. Meyer, A.W. Kleyn, L.B.F. Juurlink, RAIRS characterization of CO and O coadsorption on Cu(111), J. Phys. Chem. C. 126 (2022) 13114–13121, https://doi.org/10.1021/acs.jpcc.2c02541.

[87] D. Zhang, V. Virchenko, C. Jansen, J.M. Bakker, J. Meyer, A.W. Kleyn, I.M. N. Groot, O.T. Berg, L.B.F. Juurlink, Characterization of CO adsorbed to clean and partially oxidized Cu(211) and Cu(111), J. Phys. Chem. C. 127 (2023) 24158–24167, https://doi.org/10.1021/acs.jpcc.3c05954.

[88] K.D. Nielsen, T.E.L. Smitshuysen, C.D. Damsgaard, A.D. Jensen, J.M. Christensen, Characterization of oxide-supported Cu by infrared measurements on adsorbed CO, Surf. Sci. 703 (2021) 121725, https://doi.org/10.1016/j.susc.2020.121725.

[89] G. Escolano-Casado, S. Fatima Jafri, M. Signorile, E. Borfecchia, L. Mino, Cu-exchanged hydroxyapatites as green catalysts for CO oxidation, Catal. Sci. Technol. 15 (2025) 4194–4203, https://doi.org/10.1039/D5CY00370A.

[90] K. Hadjiivanov, H. Knozinger, FTIR study of CO and NO adsorption and coadsorption on a Cu/SiO_2 catalyst: Probing the oxidation state of copper, Phys. Chem. Chem. Phys. 3 (2001) 1132–1137, https://doi.org/10.1039/B009649K.

[91] J. Abed, I. Grigioni, T. Kose, W. Alnoush, S. Park, A. Polo, B.-H. Lee, D. Sinton, D. Higgins, E.H. Sargent, Zero-gap electrolyzers accelerate reconstruction of Cu_2O-derived catalysts under CO_2 reduction, ACS Energy Lett. 9 (2024) 6225–6232, https://doi.org/10.1021/acsenergylett.4c02634.

[92] Y. Zhong, Z. Sun, B.Y. Xia, Y. Su, Structural reconstruction of copper-based catalysts in CO_2 electroreduction reaction: A comprehensive review, Chem. A Eur. J. 31 (2025) e202500770, https://doi.org/10.1002/chem.202500770.

[93] S.H. Lee, J.E. Aviles Acosta, D. Lee, D.M. Larson, H. Li, J. Chen, J. Lee, E. Erdem, D. U. Lee, S.J. Blair, A. Gallo, H. Zheng, A.C. Nielander, C.J. Tassone, T.F. Jaramillo, W.S. Drisdell, Structural transformation and degradation of Cu oxide nanocatalysts during electrochemical CO_2 reduction, J. Am. Chem. Soc. 147 (2025) 6536–6548, https://doi.org/10.1021/jacs.4c14720.

[94] L. Debbichi, M.C. Marco de Lucas, J.F. Pierson, P. Kruger, Vibrational properties of CuO and Cu_4O_3 from first-principles calculations, and Raman and infrared spectroscopy, J. Phys. Chem. C. 116 (2012) 10232–10237, https://doi.org/10.1021/jp303096m.

[95] M. Valvo, J. Thyr, T. Edvinsson, Defect-induced Raman scattering in Cu_2O nanostructures and their photocatalytic performance, ChemElectroChem 10 (2023) e202300376, https://doi.org/10.1002/celc.202300376.

[96] T. Sander, C.T. Reindl, M. Giar, B. Eifert, M. Heinemann, C. Heiliger, P.J. Klar, Correlation of intrinsic point defects and the Raman modes of cuprous oxide, Phys. Rev. B 90 (2014) 045203, https://doi.org/10.1103/PhysRevB.90.045203.